

## Relations among net-transfer reaction progress, $^{18}\text{O}$ – $^{13}\text{C}$ depletion, and fluid infiltration in a clinohumite-bearing marble

Edward D. Young\* and Jean Morrison

Department of Geological Sciences, University of Southern California, Los Angeles, CA 90089, USA

Received May 15, 1991 / Accepted February 28, 1992

**Abstract.** A siliceous dolomitic marble xenolith within a mid-crustal Jurassic diorite exhibits mineralogical and stable isotopic evidence for infiltration of water-rich fluid. Adjacent to endoskarn which bounds the xenolith, forsterite has been replaced by clinohumite as a result of a devolatilization reaction driven by addition of aqueous fluid and extraction of heat. Isotopic compositions of calcite also record infiltration of aqueous fluid concentrated near contacts with endoskarn. Marble calcite  $\delta^{18}\text{O}_{\text{SMOW}}$  values range from +19.5‰ at the center of the xenolith to +12.6‰ adjacent to endoskarn. Calcite  $\delta^{13}\text{C}_{\text{PDB}}$  decreases sympathetically from +3.0 to +1.4‰. The calculated equilibrium composition of coexisting C–O–H–F fluid and a quantitative characterization of the whole-rock reaction which produced clinohumite and consumed graphite are used to place inequality constraints on the composition of the infiltrated fluid. Continuum mechanical transport models based on the resulting fluid compositions suggest that a small time-integrated Darcy flux of  $44 \text{ cm}^3/\text{cm}^2$  coupled with diffusive transport in the fluid was sufficient to produce both the isotopic shifts and the net-transfer reactions evidenced in the xenolith. The calculations demonstrate the importance of graphite as an indicator of time-integrated flux. The maximum possible  $\text{CH}_4$  content of the infiltrated fluid is sufficiently high to impart a 2.0‰ uncertainty in the  $\delta^{13}\text{C}$  of the fluid. The isotopic composition of the fluid is consistent with a magmatic origin when this uncertainty is taken into account.

### Introduction

The stable isotopic compositions of minerals in metamorphic rocks are influenced by the changes in mineral and fluid species proportions which result from net-

transfer reactions (Rumble 1982; Nabelek 1987; Chamberlain et al. 1990). The effects are analogous to the control that temperature (T),  $f_{\text{O}_2}$ ,  $f_{\text{S}_2}$ , and pH exert on the sulfur and carbon isotopic compositions of hydrothermal minerals (Ohmoto 1972). Thus, accurate interpretation of the causes of variations in stable isotopic compositions of metamorphic minerals requires knowledge of the reaction history of the rock.

In this study, correlation between growth of clinohumite and depletion of calcite  $^{18}\text{O}$  and  $^{13}\text{C}$  in a forsterite-bearing marble xenolith is used to examine the relations between the progress of a net-transfer reaction and changes in stable isotope ratios. A one-dimensional model for advective and diffusive fluid transport is used to explain the salient features of net-transfer reaction progress and coupled depletion of  $\delta^{18}\text{O}_{\text{Cc}}$  and  $\delta^{13}\text{C}_{\text{Cc}}$  in the marble. Results show that accurate interpretation of the stable isotope data in these high-grade marbles relies heavily on the deduced net-transfer reaction history.

### Geologic setting and petrologic description

Jurassic plutons exposed in the Mojave Desert of southeastern California, USA, typically were emplaced at shallow crustal depths of approximately 10 km or less (Young and Wooden 1988; Anderson et al. 1989). Many of these shallowly emplaced bodies were pervasively albitized during high-temperature late-magmatic interaction with meteoric aqueous fluid (Hall et al. 1988; Fox and Miller 1990). In contrast, the ca. 160 to 150 Ma plutonic complex of the Granite Mountains (Fig. 1) is composed of plutons intruded at deeper crustal levels of 18 to 25 km. Evidence for deep emplacement of these plutons includes alumina-rich igneous amphiboles in appropriate equilibrium assemblages, absence of extensive albitization, and thermochronology data (Young and Wooden 1988; Young 1990). This study of an upper Paleozoic siliceous dolomitic marble xenolith residing in the 155 Ma dioritic pluton from the Granite Mountains complex was undertaken, in part, to investigate the extent and nature of fluid-rock interaction at relatively deep crustal levels during construction of the Jurassic plutonic arc.

A cross section of the marble xenolith is shown in Fig. 2. The xenolith is bounded by an endoskarn breccia composed of epidote (Ep) + albite (Ab) + plagioclase (Pl) + K-feldspar (Kfs) + quartz (Qz)

\* Present address: Geophysical Laboratory, Carnegie Institution of Washington, 5251 Broad Branch Road NW, Washington, DC 20015-1305

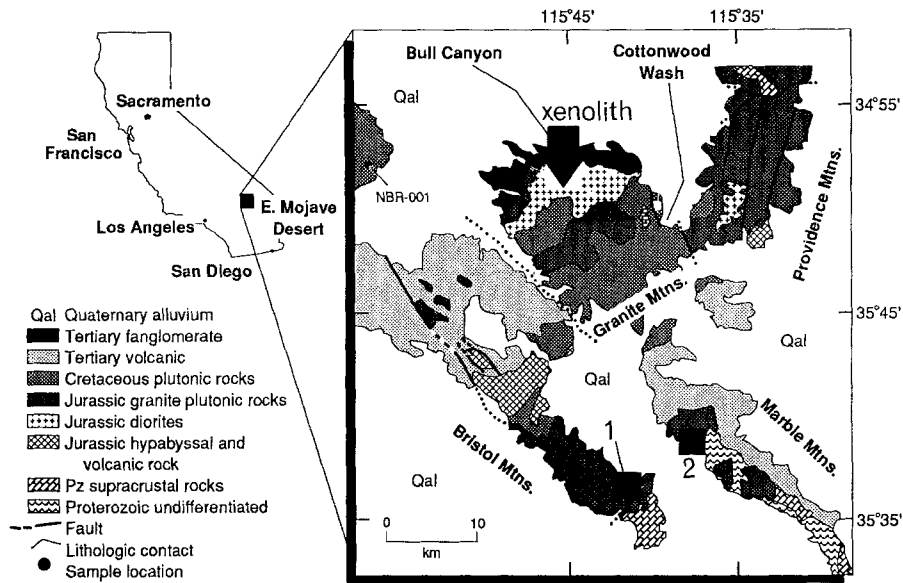


Fig. 1. Map showing the locations of Jurassic plutons of the Bristol Lake region of southeastern California. Areas 1 and 2 mark the locations of previous studies by Fox and Miller (1990) and Hall et al. (1988), which used stable isotopes to demonstrate meteoric water interaction with cooling Jurassic plutons

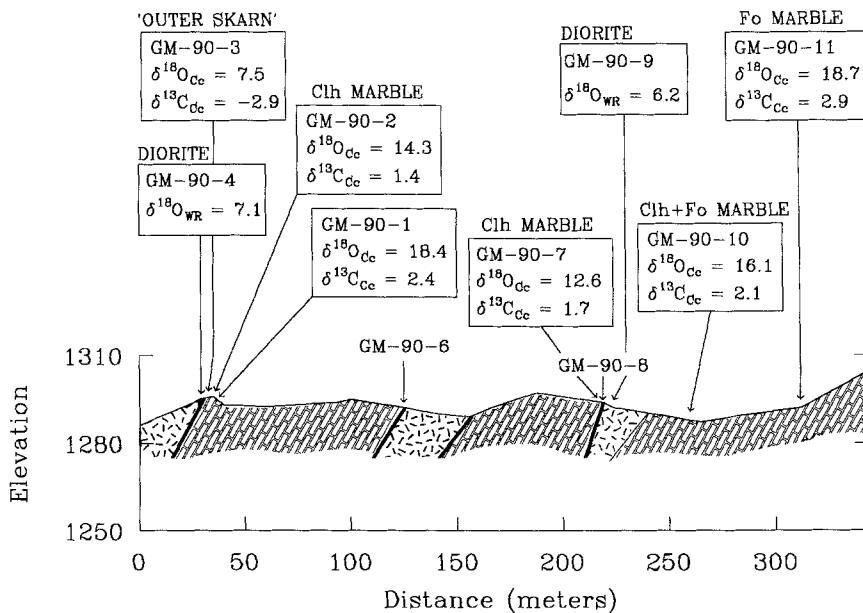


Fig. 2. Cross section of marble xenolith from the Granite Mountains showing sample locations and critical  $\delta^{18}O$  and  $\delta^{13}C$  values. Note the depleted values for  $\delta^{18}O_{Cc}$  and  $\delta^{13}C_{Cc}$  adjacent to skarn zones. Lithologic symbols: dashes: diorite; brick pattern: xenolith marble; heavy black lines: endoskarn zones. Vertical exaggeration is 1.4x

(Qz) + sphene (Sph) + calcite (Cc). Several endoskarn breccia zones also occur within the marble xenolith and are referred to throughout this paper as "inner skarns" to distinguish them from the bounding "outer skarn". Siliceous layers in the center of the marble consist of forsterite (Fo) + clinocllore (Cte) + Cc + spinel (Spn) + dolomite (Do) + graphite (Gr) with rare clinohumite and rutile. Clinocllore partially replaces forsterite. In the vicinity of skarn zones, Fo has been replaced by clinohumite (Clh). Rare humite (Hu) is also found associated with Clh adjacent to skarns. Replacement of Fo by humite minerals is accompanied by a marked decrease in Spn and Do and complete loss of Gr. Increase in the abundance of Cte at the endoskarn contacts is required by mass balance (Spn is the only other alumina phase in the marbles) but is difficult to document petrographically. The term "margin" as applied to the xenolith is used to refer to the contact with the outer skarn.

### Mineral chemistry

Wavelength dispersive electron microprobe analyses and energy dispersive scans show that of the phases present in the marble

xenolith, only clinohumite, humite, and clinocllore exhibit significant deviations from end member compositions. Compositions are described below.

### Analytical methods

Mineral compositions for sample GM-90-11, which represents the center of the xenolith, and samples GM-90-1 and GM-90-2, representing the xenolith margin, were obtained using the wavelength dispersive Cameca SX automated electron microprobe at the University of California, Los Angeles. Accelerating voltage was 15 kV and spot size varied from 10 to 20  $\mu\text{m}$ . Data reduction was performed with a ZAF correction scheme which included F and Cl. TAP and PET analyzer crystals were used for F and Cl analyses, respectively. The F standard was a synthetic fluorophlogopite containing 9.02 wt.% F. The Cl standard consisted of a barium chlorapatite with 3.52 wt.% Cl. Standards for other elements consisted of natural and synthetic minerals and glasses. Reported analyses represent averages of data from 2 or 3 closely spaced analysis spots.

**Table 1.** Electron microprobe analyses of representative chlorites

Sample	GM-90-11 pt3	GM-90-11 pt6	GM-90-2 pt15	GM-90-2 pt23	GM-90-1 pt30	GM-90-1 pt32
Weight per cent						
SiO <sub>2</sub>	31.6	30.3	31.8	30.7	30.5	30.6
Al <sub>2</sub> O <sub>3</sub>	17.6	20.7	18.8	19.7	20.5	20.7
TiO <sub>2</sub>	0.02	0.10	0.02	0.00	0.02	0.03
Cr <sub>2</sub> O <sub>3</sub>	0.00	0.00	0.00	0.17	0.15	0.22
FeO <sup>a</sup>	0.13	0.14	0.63	0.65	0.19	0.22
MnO	0.00	0.00	0.00	0.03	0.01	0.01
MgO	37.7	35.2	35.7	35.0	35.0	34.7
CaO	0.07	0.04	0.05	0.03	0.01	0.05
Na <sub>2</sub> O	0.00	0.02	0.00	0.00	0.00	0.01
K <sub>2</sub> O	0.01	0.00	0.00	0.01	0.01	0.00
F	0.28	0.06	0.31	0.18	0.19	0.13
Cl	0.02	0.01	0.00	0.02	0.02	0.01
H <sub>2</sub> O <sup>b</sup>	12.8	12.8	12.8	12.7	12.7	12.8
Total	100.1	99.3	100.1	99.2	99.4	99.6
O = F + Cl	0.12	0.03	0.13	0.08	0.09	0.06
Total	100.0	99.3	99.9	99.1	99.3	99.5
18(O, OH, F, Cl)						
Si	2.934	2.830	2.958	2.877	2.851	2.855
Al <sup>IV</sup>	1.066	1.170	1.042	1.123	1.149	1.145
Al <sup>VI</sup>	0.857	1.106	1.016	1.058	1.109	1.130
Ti	0.001	0.007	0.001	0.000	0.001	0.002
Cr <sup>3+</sup>	0.000	0.000	0.000	0.013	0.011	0.016
Fe <sup>2+*</sup>	0.010	0.011	0.049	0.051	0.015	0.017
Mn	0.000	0.000	0.000	0.002	0.001	0.001
Mg	5.226	4.897	4.940	4.898	4.874	4.824
Ca	0.007	0.004	0.005	0.003	0.001	0.005
Na	0.000	0.004	0.000	0.000	0.000	0.002
K	0.001	0.000	0.000	0.001	0.001	0.000
F	0.082	0.018	0.091	0.053	0.056	0.038
Cl	0.003	0.002	0.000	0.003	0.003	0.002
OH <sup>b</sup>	7.915	7.980	7.909	7.944	7.941	7.960

<sup>a</sup> Total Fe (\*)

<sup>b</sup> Calculated assuming stoichiometric hydroxyl site occupancy

Concentrations of H<sub>2</sub>O were calculated assuming stoichiometric occupancy of hydroxyl sites by OH, F, and Cl.

### Chlorite and humite mineral chemistry

Chlorites deviate from end-member clinocllore due to greater total Al per formula unit (Table 1). Excess Al is greater in the tetrahedral sites than in the octahedral sites. Replacement of Al<sup>VI</sup> by Fe<sup>3+</sup> and Cr<sup>3+</sup> is limited. The average mole fraction of OH on the chlorite hydroxyl site exceeds 0.99 (Table 1).

Clinohumites contain significant concentrations of Ti and F (Table 2). Approximately 50% of the hydroxyl sites are occupied by F ( $X_F^{Clh} \approx 0.5$ ) and up to 1.5% of the octahedral sites contain Ti. Humites are distinguished from clinohumites on the basis of stoichiometry and are easily recognized in these rocks by their high weight concentrations of F (Table 3). Both Ti and  $X_F^{Hu}$  are similar to the values in associated Clh. Similarity in  $X_F^{Clh}$  and  $X_F^{Hu}$  is consistent with the lack of partitioning of F evidenced in the manganese analogues of these phases (Winter et al. 1983).

Concentrations of Ti and F in the clinohumites are typical of occurrences in silica-undersaturated siliceous carbonates (Rice 1980; Ribbe 1982). There is a decrease in average Ti per 13 cation formula from 0.142 at the center of the xenolith to 0.009 at the

margin (Table 2).  $X_F^{Clh}$  is slightly higher on average at the center of the xenolith compared to samples at the margin, but the 10% variation is of questionable significance since it is similar to the range found across individual polished sections. Humite compositions show negligible variability.

### CO<sub>2</sub>–H<sub>2</sub>O fluid calculations

Initially, insight into the nature of fluid-rock interactions responsible for growth of clinohumite and attendant heavy isotope depletion in Cc in the marble xenolith is obtained by performing phase equilibria and isotope fractionation calculations assuming a mixed CO<sub>2</sub>–H<sub>2</sub>O binary fluid. This starting place is illustrative because of the prevalence of the assumption of a binary fluid in many stable isotope and petrological studies (e.g., Baker et al. 1989). Phase equilibria and isotope relationships elucidated with the binary-fluid calculations form the foundation for more detailed discussions which incorporate fluid calculations in the C–O–H–F system.

**Table 2.** Electron microprobe analyses of representative clinohumites

Sample	GM-90-11 pt4	GM-90-11 pt9	GM-90-11 pt12	GM-90-2 pt20	GM-90-2 pt21	GM-90-2 pt22	GM-90-2 pt25	GM-90-1 pt28
Weight per cent								
SiO <sub>2</sub>	38.5	38.1	39.0	39.2	39.0	38.8	39.0	39.4
TiO <sub>2</sub>	2.11	1.29	2.07	0.13	0.14	0.07	0.11	0.19
FeO <sup>a</sup>	0.52	0.46	0.43	1.00	1.00	0.97	0.99	0.44
MnO	0.06	0.02	0.04	0.04	0.04	0.04	0.03	0.05
MgO	57.1	57.4	57.4	57.8	58.0	57.9	58.1	58.7
CaO	0.01	0.12	0.04	0.02	0.04	0.01	0.03	0.07
F	2.19	2.94	2.50	3.03	3.00	2.95	3.06	3.53
Cl	0.00	0.01	0.00	0.00	0.01	0.01	0.00	0.00
H <sub>2</sub> O <sup>b</sup>	1.38	1.20	1.27	1.45	1.46	1.49	1.45	1.22
Total	101.8	101.5	102.8	102.7	102.8	102.3	102.8	103.6
O = F + Cl	0.92	1.24	1.05	1.28	1.27	1.25	1.29	1.49
Total	100.9	100.3	101.7	101.5	101.5	101.0	101.5	102.1
13 cations								
Si	3.983	3.960	4.002	4.032	4.009	4.004	4.003	4.021
Ti	0.164	0.101	0.160	0.01	0.011	0.005	0.008	0.015
Fe <sup>2+*</sup>	0.045	0.04	0.037	0.086	0.086	0.084	0.085	0.038
Mn	0.005	0.002	0.003	0.003	0.003	0.004	0.003	0.004
Mg	8.802	8.885	8.793	8.863	8.886	8.901	8.897	8.915
Ca	0.001	0.013	0.004	0.002	0.004	0.001	0.003	0.008
F	0.717	0.966	0.812	0.985	0.975	0.962	0.994	1.138
Cl	0.000	0.002	0.000	0.000	0.002	0.002	0.000	0.000
OH <sup>b</sup>	0.955	0.830	0.868	0.995	1.001	1.026	0.990	0.832
R <sup>c</sup>	8.960	8.905	9.005	9.077	9.022	9.010	9.007	9.050
X <sub>F</sub>	0.429	0.537	0.483	0.497	0.493	0.483	0.501	0.578

<sup>a</sup> Total Fe (\*)<sup>b</sup> Stoichiometric based on ordering of Ti to M3 (Ribbe 1982)<sup>c</sup>  $R = 2\text{Si}/[2n/\Sigma R^{\text{VI}}]$ ,  $n = (\Sigma R^{\text{VI}} - 1)/2$ , stoichiometric clinohumite yields  $R = 9.000$ 

### *T* - *X*<sub>CO<sub>2</sub></sub> phase equilibria

An isobaric *T* - *X*<sub>CO<sub>2</sub></sub> phase diagram which includes the phases found in the marble xenolith is shown in Fig. 3. The diagram was constructed using the equilibrium constant expressions of Rice (1980). These values were used in Fig. 3 because they were refined by Rice to yield topologies consistent with observed parageneses in aluminous silica-undersaturated dolomitic marbles. Since humite is a likely low-temperature late-stage replacement of Clh (Rice 1980; Winter et al. 1983) it has been excluded from these calculations. The binary CO<sub>2</sub> - H<sub>2</sub>O fluid phase was modeled using the hard-sphere modified Redlich-Kwong (HSMRK) equations of state and the non-ideal mixing rule of Kerrick and Jacobs (1981). Constant activities of solid components were used. Activities of hydroxyl and fluor-clinohumite were calculated using the subregular solution model of Duffy and Greenwood (1979). The activities of Cc and Do are fixed by the calcite-dolomite solvus using the equations given by Skippen (1974). Clinocllore activity was calculated with an ideal mixing-on-sites configurational expression which excludes the tetrahedral sites as recommended by Bryndzia and Scott (1984).

Geobarometry suggests diorite crystallization pressures of approximately 6 kb (Young and Wooden 1988) and this pressure was used in Fig. 3. The Clh composition used is representative of those found in the xenolith. It is clear from Fig. 3 that coexistence of Cc and Clh requires exceedingly water-rich fluid conditions irrespective of solid solution. The assemblage Cc + Cte + Clh + Do + Fo + Spn found throughout most of the xenolith defines the isobaric diopside-tremolite-absent invariant point located at 600 °C and an *X*<sub>CO<sub>2</sub></sub> of 0.02 for the specified Clh composition. A minimum *X*<sub>CO<sub>2</sub></sub> for the marbles is suggested by the lack of brucite which forms at the expense of Do under extremely water-rich conditions (Rice 1980). The limited variability in clinohumite and chlorite composition results in negligible displacement of the isobaric invariant point from the position shown in Fig. 3, permitting the approximation that Cc + Cte + Clh + Do + Fo + Spn was an invariant assemblage in these rocks. This approximation remains valid in the context of the more complete phase-equilibria analysis presented below. The effects of pressure are minimal; recalculation of the diagram in Fig. 3 at 2 kb causes only a minor shift in the position of the invariant point to a temperature of 570 °C and an *X*<sub>CO<sub>2</sub></sub> of 0.06 (Fig. 3).

GM-90-1 pt29	GM-90-1 pt31	GM-90-1 pt33
38.9	39.0	39.1
0.18	0.21	0.20
0.41	0.42	0.45
0.04	0.04	0.02
58.1	58.8	58.6
0.03	0.03	0.05
3.17	3.20	3.35
0.01	0.01	0.01
1.36	1.37	1.30
102.2	103.1	103.1
1.34	1.35	1.41
100.9	101.8	101.7
4.010	3.984	3.996
0.014	0.016	0.015
0.035	0.036	0.038
0.003	0.003	0.002
8.931	8.955	8.941
0.003	0.003	0.005
1.034	1.034	1.084
0.002	0.002	0.002
0.936	0.932	0.884
9.024	8.962	8.991
0.524	0.525	0.550

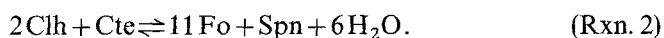
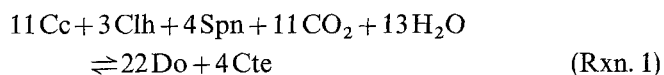
**Table 3.** Electron microprobe analyses of representative humites

Sample	GM-90-2 pt16	GM-90-2 pt17	GM-90-2 pt18
Weight per cent			
SiO <sub>2</sub>	37.8	37.7	37.7
TiO <sub>2</sub>	0.22	0.16	0.27
FeO <sup>a</sup>	0.89	0.79	0.83
MnO	0.07	0.03	0.03
MgO	58.6	58.4	58.4
CaO	0.02	0.03	0.02
F	4.23	4.24	4.30
Cl	0.00	0.00	0.00
H <sub>2</sub> O <sup>b</sup>	1.73	1.72	1.67
Total	103.6	103.0	103.1
O=F+Cl	1.78	1.79	1.81
Total	101.8	101.2	101.3
10 cations			
Si	2.994	3.001	2.997
Ti	0.013	0.009	0.016
Fe <sup>2+*</sup>	0.059	0.053	0.055
Mn	0.005	0.002	0.002
Mg	6.927	6.932	6.927
Ca	0.002	0.003	0.002
F	1.060	1.069	1.083
Cl	0.000	0.000	0.000
OH <sup>b</sup>	0.914	0.913	0.885
R <sup>c</sup>	6.985	7.001	6.993
X <sub>F</sub>	0.537	0.539	0.550

<sup>a</sup> Total Fe (\*)<sup>b</sup> Stoichiometric based on ordering of Ti to M3 (Ribbe 1982)<sup>c</sup>  $R = 2Si/[2n/\Sigma R^{VI}]$ ,  $n = (\Sigma R^{VI} - 1)/2$ , stoichiometric humite yields  $R = 7.000$ 

### Net-transfer reaction history

The net-transfer reactions which can take place at the isobaric invariant point in Fig. 3 and the factors which drive them are revealed in the reaction progress diagram in Fig. 4. Ferry (1983) presented a detailed discussion of the construction and interpretation of reaction progress diagrams (see also Thompson et al. 1982). All possible reactions at the invariant point are fully described by any two linearly independent reactions which intersect at the point. The two reactions used for this purpose in Fig. 4 are:



Reaction 1 (Rxn. 1) and Rxn. 2 are labeled [Fo] and [Do, Cc], respectively, in Fig. 3. Change in the amount of Do defines progress of Rxn. 1 ( $\xi_1$ ), serving as a monitor of the extent of Rxn. 1 relative to a specified initial state and bulk composition. Similarly, the amount of Fo defines progress of Rxn. 2 ( $\xi_2$ ). Construction of Fig. 4

required assignment of initial proportions of phases and a bulk composition to represent the system before extensive progress of reactions at the invariant point. The mineral proportions and bulk composition of sample GM-90-11 were used to define these initial conditions. GM-90-11 is the sample furthest removed from the boundaries of the xenolith, contains the least amount of humite minerals, and has the highest  $\delta^{18}\text{O}_{\text{Cc}}$  and  $\delta^{13}\text{C}_{\text{Cc}}$ . The mineral proportions of sample GM-90-11 and the indicated equilibrium conditions therefore correspond to the origin in Fig. 4 and all parameters shown are referenced to 1000 cm<sup>3</sup> of rock of this bulk composition.

Complete consumption of Do in a rock of the same bulk composition as sample GM-90-11 is represented by the horizontal bounding line labeled [Do] in Fig. 4. Similarly, the bounding line labeled [Fo] marks the complete consumption of Fo resulting from progress of Rxn. 2 in the negative direction ( $-\xi_2$ , right to left as written earlier) from the origin. The bounding lines labeled [Clh] and [Spn] correspond to losses of Clh and Spn, respectively.

Within the reaction-space polyhedron defined by these boundaries there are four special reaction progress

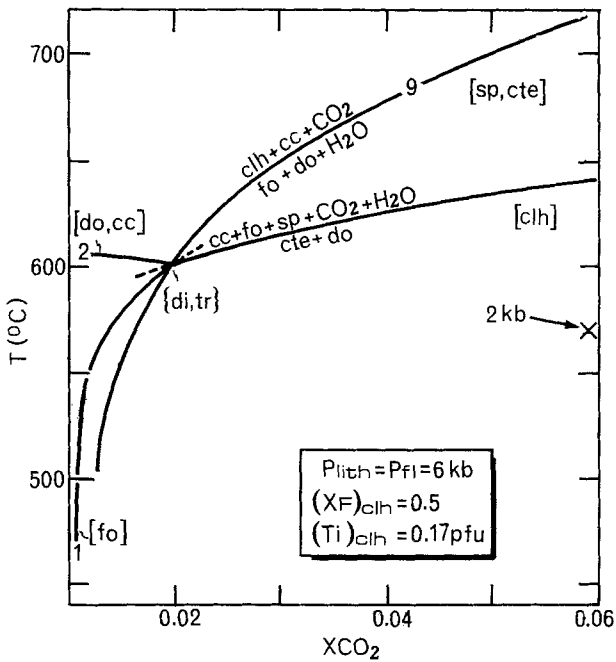


**Fig. 3.** Calculated isobaric  $T-X_{\text{CO}_2}$  phase diagram for the system  $\text{CaO}-\text{MgO}-\text{SiO}_2-\text{Al}_2\text{O}_3-\text{CO}_2-\text{H}_2\text{O}-\text{HF}$  at constant solid component activities described in the text. Note the water-rich conditions required for  $\text{Clh}+\text{Cc}$  stability. Reactions 1, 2, and 9 are discussed in the text. The position of the diopside-tremolite-absent invariant point ( $\{\text{di}, \text{tr}\}$ ) at 2 kb is also shown. See Rice (1980) for a detailed discussion of topologies in this system

paths (Fig. 4). Two of these paths, labeled  $-Q$  and  $+Q$  (arrows on Fig. 4), show trajectories corresponding to reactions which occur in response to a withdrawal or addition of heat (isobaric changes in system enthalpy), respectively, without interaction with an external fluid. The other two, labeled  $+H_2O$  and  $+CO_2$ , depict the trajectories of isoenthalpic reactions induced by interaction with fluids with higher concentrations of  $H_2O$  or  $CO_2$ , respectively, relative to the equilibrium fluid composition. Reaction progress from the origin in directions other than these four paths requires both infiltration of fluid and loss or gain of heat. Contours are shown for the volume of  $\text{Clh}$  and the change in heat energy per  $1000 \text{ cm}^3$  of rock. A loss of 100 kJ of heat in this diagram is equivalent to a decrease in temperature of  $31^\circ\text{C}$  if the rock were composed entirely of  $\text{Cc}$  and no reactions were permitted to take place.

The proportions of mineral phases among rocks of the same bulk composition as sample GM-90-11 record progress of reactions depicted in Fig. 4 based on their relative positions in the reaction space. X-ray fluorescence analyses were used to identify those samples which have the same bulk composition as GM-90-11. Three of the rocks examined have bulk compositions similar to GM-90-11 and are plotted in Fig. 4. Relative amounts of  $\text{Do}$  and  $\text{Fo}$  in these samples were determined from X-ray diffraction data normalized to a prominent  $\text{Cc}$  peak and were used to estimate  $\xi_1$  and  $\xi_2$ .

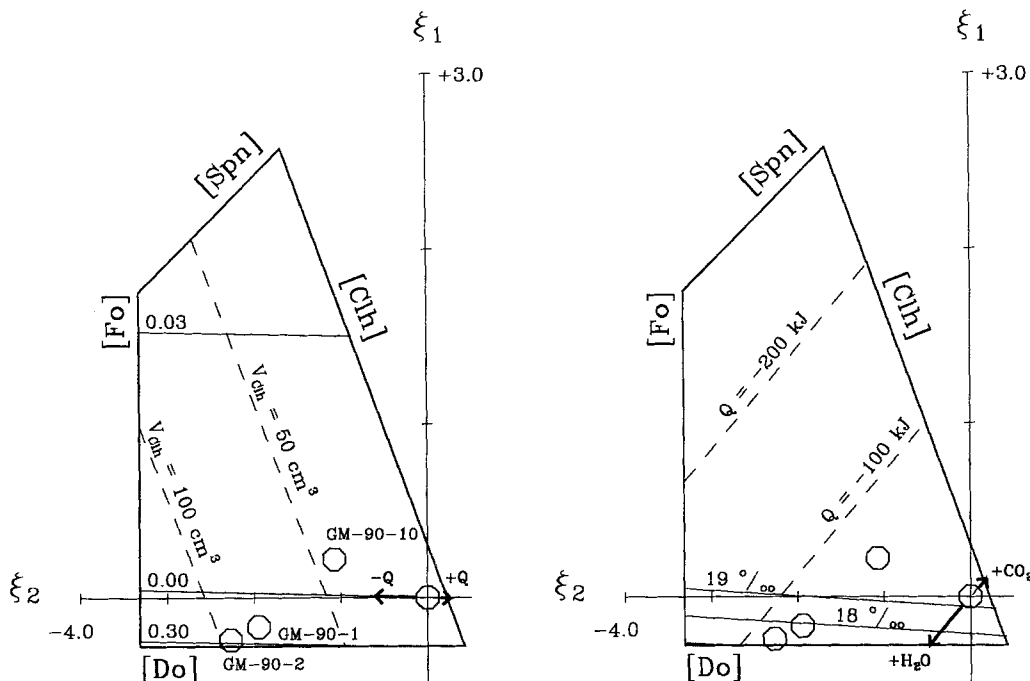


**Fig. 4.** Net-transfer reaction progress diagrams for the  $\{\text{di}, \text{tr}\}$  invariant point in Fig. 3. Sample GM-90-11 is represented by the origin, and all parameters are referenced to  $1000 \text{ cm}^3$  of rock. The bounding lines labeled  $[\text{Fo}]$ ,  $[\text{Do}]$ ,  $[\text{Spn}]$ , and  $[\text{Clh}]$  complete consumption of the indicated phases by reaction. Left: Solid contours show volumetric fluid-rock ratios for pure  $H_2O$  and pure  $CO_2$  below and above the 0.0 line, respectively. Dashed contours show

the volume of clinohumite. Numbered octagons show the reaction progress recorded by the indicated samples. Right: Solid contours show changes in  $\delta^{18}\text{O}_{\text{Cc}}$  attending reaction for the zero-dimensional model described in the text. Dashed contours show changes in system enthalpy based on  $\Delta \hat{H}^{1b,600^\circ\text{C}}$  of  $-76.617 \text{ kJ/mole Do}$  and  $45.108 \text{ kJ/mole Fo}$  for reactions 1 and 2, respectively. The heavy arrows are discussed in the text

This procedure eliminated difficulties in distinguishing Clh from Fo optically.

Sample GM-90-2 is a marble collected approximately 20 cm from the outer skarn contact. Sample GM-90-1 was collected at a distance of approximately 50 cm from the contact. The positions of the two margin samples in Fig. 4 indicate that Clh grew in response to both loss of heat and infiltration of H<sub>2</sub>O-rich fluid. The clinohumite-producing reaction at the invariant point involved consumption of Fo, Do, and Spn and production of Cte. The predicted lower modal Spn content at the margin relative to the center of the xenolith is confirmed by petrographic observations. Sample GM-90-10 was collected approximately 60 m from GM-90-11 towards the outer skarn contact well within the interior of the xenolith (Fig. 2). This sample records a decrease in heat similar to that at the margin but its mineral proportions suggest that it was infiltrated by a more CO<sub>2</sub>-rich fluid.

### Zero-dimensional infiltration model

A minimum estimate of the integrated volume of mixed CO<sub>2</sub>-H<sub>2</sub>O fluid required to produce the observed reaction progress at the margin of the xenolith can be obtained by assuming the fluid was pure H<sub>2</sub>O and that it all reacted with the same volume of rock (i.e., a zero-dimensional, or "box" model in the terminology of Blattner and Lassey 1990 and Ferry 1991). Isopleths for volumetric fluid-rock ratio based on these assumptions indicate that addition of approximately 0.3 rock volumes of pure H<sub>2</sub>O could have produced the observed Clh (Fig. 4). However, the integrated amount of infiltrated fluid is a direct function of its composition, and the in toto interaction between fluid and rock implied by the fluid-rock ratio is unlikely in natural systems (Baumgarnter and Rumble 1988). These shortcomings are overcome below by examination of the fluid compositions in the C-O-H-F system, and, following presentation of the isotope data, by application of the tenets of continuum mechanics to derive more realistic constraints on the amount of fluid which infiltrated the marble and the mechanisms of fluid transport.

### C-O-H-F fluid calculations

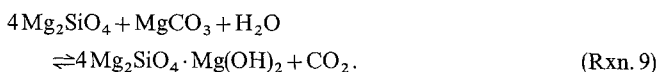
Equilibrium fluid compositions defined by the assemblage Fo + Clh + Do + Cc + Gr were calculated as functions of temperature and Clh composition. Ohmoto and Kerrick (1977) noted that isobaric invariant assemblages containing graphite which define high  $X_{\text{CO}_2}^{\text{Eq}}$  equilibrate with essentially binary CO<sub>2</sub>-H<sub>2</sub>O fluids, while those which define low  $X_{\text{CO}_2}^{\text{Eq}}$  equilibrate with fluids containing appreciable CH<sub>4</sub>. From these observations, the requirement of low  $X_{\text{CO}_2}$ , and the presence of Gr in parts of the xenolith it is clear that the H<sub>2</sub>O-CO<sub>2</sub> system is inadequate for depiction of the fluids in this study. The fluids were therefore modeled in the C-O-H-F system.

### Methods and thermochemical data

At the P and T of interest in this study, supercritical fluids in the C-O-H-F system can be considered to be entirely associated (Holloway 1987). The fugacities of the 8 principal species in such a fluid are related to one another at equilibrium by the 4 homogeneous equilibria:



Equilibration with Gr, Fo, Do, Cc, and Clh imposes three additional constraints among the fluid species through 3 heterogeneous equilibria:



This trivariant assemblage is analogous to the [Spn, Cte] univariant assemblage in Fig. 3 at constant pressure and Clh composition. An additional constraint relating fluid fugacities is based on the assumption that the total fluid pressure was equivalent to the lithostatic pressure  $P_L$ , yielding:

$$P_L = \frac{f_{\text{H}_2\text{O}}}{\gamma_{\text{H}_2\text{O}}} + \frac{f_{\text{CO}_2}}{\gamma_{\text{CO}_2}} + \frac{f_{\text{CH}_4}}{\gamma_{\text{CH}_4}} + \frac{f_{\text{CO}}}{\gamma_{\text{CO}}} + \frac{f_{\text{H}_2}}{\gamma_{\text{H}_2}} + \frac{f_{\text{HF}}}{\gamma_{\text{HF}}} + \frac{f_{\text{O}_2}}{\gamma_{\text{O}_2}} + \frac{f_{\text{F}_2}}{\gamma_{\text{F}_2}} \quad (1)$$

where  $f_i$  are the fugacities of fluid species  $i$  referenced to a standard state of pure ideal gas at 1 bar and temperature of interest and  $\gamma_i$  are the fugacity coefficients for species  $i$ .

Equilibria involving Cte and Spn were not included in these calculations so that conditions for stable coexistence of Clh and Cc other than the isobaric invariant point in Fig. 3 could be considered. Such conditions could be represented in the marble xenolith if, for example, the relatively sparse Spn at the margin were interpreted to mean that this phase was effectively exhausted early in the reaction history by Cte-producing reactions. In this case Clh could have grown polythermally by Rxn. 9.

The equilibrium constant expressions for Reactions 3-9 and Eq. (1) comprise a system of 8 non-linear equations which were solved simultaneously using a Newton-Raphson iteration method to define equilibrium values for  $\log f_i$  at specified P, T, and activities of solid species. Activities of the hydroxyl and fluor-clinohumite components were calculated as:

$$a_{\text{OH-clh}} = (X_{\text{Mg}}^{\text{M1,M2}})^8 (X_{\text{Mg}}^{\text{M3}}) (X_{\text{OH}})^{2-2x} \lambda_{\text{OH}} \\ a_{\text{F-clh}} = (X_{\text{Mg}}^{\text{M1,M2}})^8 (X_{\text{Mg}}^{\text{M3}}) (X_{\text{F}})^{2-2x} \lambda_{\text{F}} \quad (2)$$

where  $\lambda_{\text{OH}}$  and  $\lambda_{\text{F}}$  are the subregular activity coefficients of Duffy and Greenwood (1979),  $x$  represents moles per formula unit of Ti, and the ideal contributions to the activities are mixing-on-sites formulations with Ti assigned to M3 (see Appendix). Activity of MgCO<sub>3</sub> was defined by the Do-Cc solvus and the activity-composition expression of Gordon and Greenwood (1970). Gr and Fo are pure phases and define unit activities. Graphite-absent assemblages were modeled by assigning a low arbitrary carbon activity of 0.01 for comparison with graphite-bearing assemblages (Lamb and Valley 1985).

Fugacity coefficients for CH<sub>4</sub>, CO<sub>2</sub>, and H<sub>2</sub>O were calculated

using the HSMRK equations of state for these species presented by Kerrick and Jacobs (1981) and Jacobs and Kerrick (1981) and the non-ideal mixing rules used by these workers. Fugacity coefficients for CO and H<sub>2</sub> were taken from the corresponding states best-fit expressions of Naumov et al. (1971). All other  $\gamma_i$  were assumed to be 1.

Equilibrium constant expressions were obtained using apparent molar enthalpies of formation of pure species ( $\Delta_a \hat{H}^{P,T}$ ), third-law entropies ( $\hat{S}^{P,T}$ ), and molar volumes of solid phase components ( $\hat{V}^{1,298}$ ) calculated from the standard state thermochemical data and heat capacity equations of Berman (1988) wherever possible. Thermochemical properties of fluid species not included in the Berman data base were calculated using the standard state data and heat capacity equations of Robie et al. (1979) for CO, O<sub>2</sub>, H<sub>2</sub>, CH<sub>4</sub>, and F<sub>2</sub> and Stull and Prophet (1971) for HF. Data common to each of the sources used for fluid species are consistent to within less than 0.06%. Graphite  $\Delta_a \hat{H}^{P,T}$ ,  $\hat{S}^{P,T}$ , and  $\hat{V}^{1,298}$  were taken from Robie et al. (1979). Compressibility and expansivity for graphite were calculated from data in Birch (1966) and Skinner (1966).

Clinohumite  $\Delta_a \hat{H}^{P,T}$  compatible with the thermochemical data for the other phases were derived by translating the Gibbs free energies of formation of hydroxyl and fluor-clinohumite from MgO, MgF<sub>2</sub>, SiO<sub>2</sub>, and H<sub>2</sub>O at 1023 K ( $\Delta_r \hat{G}^{1,1023}$ ) given by Duffy and Greenwood (1979) into the Berman (1988) data base with the relation:

$$\Delta_r \hat{H}^{1,298} = \Delta_r \hat{G}^{1,1023} - \int_{298}^{1023} \Delta_r \hat{C}_p dT + 1023 \left( \Delta_r \hat{S}^{1,298} + \int_{298}^{1023} \frac{\Delta_r \hat{C}_p}{T} dT \right) \quad (3)$$

where the entropy and heat capacity data for MgO, SiO<sub>2</sub>, H<sub>2</sub>O, and the  $\alpha$ - $\beta$  transition in quartz necessary to evaluate the integrals in Eq. (3) were taken from Berman (1988). Parameters for MgF<sub>2</sub> (sellaite) are from Robie et al. (1979). Enthalpies of formation from the elements for the Clh components were derived from  $\Delta_r \hat{H}^{1,298}$  using reference state values from Berman and Robie et al. The translated  $\Delta_r \hat{H}^{1,298}$  for hydroxyl and fluor-clinohumite are  $-9632.986 \text{ kJ mol}^{-1}$  and  $-9834.027 \text{ kJ mol}^{-1}$ , respectively. Heat capacity equations, third-law entropies, and molar volumes for Clh components were taken from Duffy and Greenwood (1979).

## Results

The calculated equilibrium fluid compositions at 600 °C for samples GM-90-11, representing the graphitic interior of the xenolith, and GM-90-1 and GM-90-2, representing the margin of the xenolith, are summarized in Table 4. The results under Gr-saturated conditions as a function of temperature and  $X_F^{\text{Clh}}$  are shown in Fig. 5. Shifts in  $X_{\text{CO}_2}^{\text{Eq}}$  as a result of lowering the activity of carbon from 1 (Gr saturation) to 0.01 are  $\ll 0.01$  at constant  $X_F^{\text{Clh}}$  and  $T$ . As a result, if temperature was nearly constant, as suggested by equilibrium with Cte and Spn of uniform composition (e.g., Fig. 3),  $X_{\text{CO}_2}^{\text{Eq}}$  was nearly constant, ranging from 0.03 to 0.05 across the xenolith. As with the binary-fluid calculations, nearly uniform  $X_F^{\text{Clh}}$  permits the approximation that the assemblage Cc+Cte+Clh+Do+Fo+Spn represents an isobaric invariancy in  $T$ - $X_{\text{CO}_2}$  space. Clh could have also been produced, at least in part, by Rxn. 9 if the paucity of Spn at the margin of the xenolith is indicative of its consumption to form Cte before exhaustion of

**Table 4.** Calculated fluid compositions at 6 kbar and 600 °C in equilibrium with Fo+Clh+Do+Cc±graphite in the system C-O-H-F<sup>a</sup>

	GM-90-11 <sup>b</sup>	GM-90-1 <sup>c</sup>	GM-90-2 <sup>d</sup>
$X_F^{\text{Clh}}$	0.483	0.544	0.506
$a_{\text{OH-Clh}}^e$	0.165	0.118	0.163
$a_C^f$	1.000	0.010	0.010
$\log f_{\text{O}_2}$	-20.127	-17.982	-18.118
$\gamma_{\text{O}_2}$	1.000	1.000	1.000
$\log f_{\text{CO}_2}$	3.732	3.877	3.741
$\gamma_{\text{CO}_2}$	26.348	25.700	27.691
$\log f_{\text{CO}}$	1.432	0.504	0.437
$\gamma_{\text{CO}}$	8.966	8.966	8.966
$\log f_{\text{H}_2}$	1.716	0.642	0.716
$\gamma_{\text{H}_2}$	3.958	3.958	3.958
$\log f_{\text{H}_2\text{O}}$	3.589	3.587	3.593
$\gamma_{\text{H}_2\text{O}}$	0.677	0.678	0.675
$\log f_{\text{CH}_4}$	3.273	-0.875	-0.728
$\gamma_{\text{CH}_4}$	38.362	37.391	40.713
$\log f_{\text{HF}}$	-1.499	-1.296	-1.442
$\gamma_{\text{HF}}$	1.000	1.000	1.000
$\log f_{\text{F}_2}$	-37.951	-36.471	-36.836
$\gamma_{\text{F}_2}$	1.000	1.000	1.000

<sup>a</sup> Fugacities are in bars; calculations based on  $a_{\text{CaCO}_3}^{\text{Cc}} = 0.929$  and  $a_{\text{MgCO}_3}^{\text{Cc}} = 0.417$  (see text)

<sup>b</sup> Sample represents graphitic interior of xenolith

<sup>c</sup> Sample collected 50 cm from outer skarn contact

<sup>d</sup> Sample collected 20 cm from outer skarn contact

<sup>e</sup>  $a_{\text{OH-Clh}}$  = average activity of  $4\text{Mg}_2\text{SiO}_4 \cdot \text{Mg}(\text{OH})_2$  in Clh

<sup>f</sup> Activity of carbon defined by presence or absence of graphite (see text)

Fo.  $X_{\text{CO}_2}^{\text{Eq}}$  and temperature would then have been constrained by the curves in Fig. 5.

In the presence of graphite, relatively constant  $X_F^{\text{Clh}}$  suggests a restricted range in  $f_{\text{O}_2}$  (Fig. 6). Rice (1980) argued that growth of Clh in response to infiltration of pure H<sub>2</sub>O should result in a progressive decrease in  $X_F^{\text{Clh}}$ . Figure 6 illustrates that under isothermal-isobaric conditions, presence of Gr throughout much of the Clh growth history could have buffered fluid  $f_{\text{O}_2}$  during infiltration, resulting in the observed uniform  $X_F^{\text{Clh}}$ . At the margin of the xenolith where Gr is absent,  $f_{\text{O}_2}$  may have been higher than the graphite-saturation surface by as much as 2 log units ( $\log f_{\text{O}_2} = -18$ ) at 600 °C with no change in  $X_F^{\text{Clh}}$ , based on calculations at carbon activities of 0.01. The significance of the absence of Gr at the margin of the xenolith is most evident when cast in terms of reduced *versus* oxidized carbon. The equilibrium fraction of total carbon ( $\Sigma\text{C}$ ) associated with CH<sub>4</sub> ( $X_{\text{CH}_4}^{\Sigma\text{C}}$ ) in the fluid phase is between 0.1 and 0.5 at 700 °C to 500 °C, respectively, in the graphitic assemblage despite low mole fractions of CH<sub>4</sub> on the order of  $8 \times 10^{-3}$  (Table 4). The buffered  $X_{\text{CH}_4}^{\Sigma\text{C}}$  for the graphite-absent assemblages is negligible. This variability in  $X_{\text{CH}_4}^{\Sigma\text{C}}$  has profound effects on the carbon isotope systematics of the system (see below).

The  $\log f_{\text{HF}}$  recorded in these rocks are identical to those obtained for similar conditions by Valley et al.

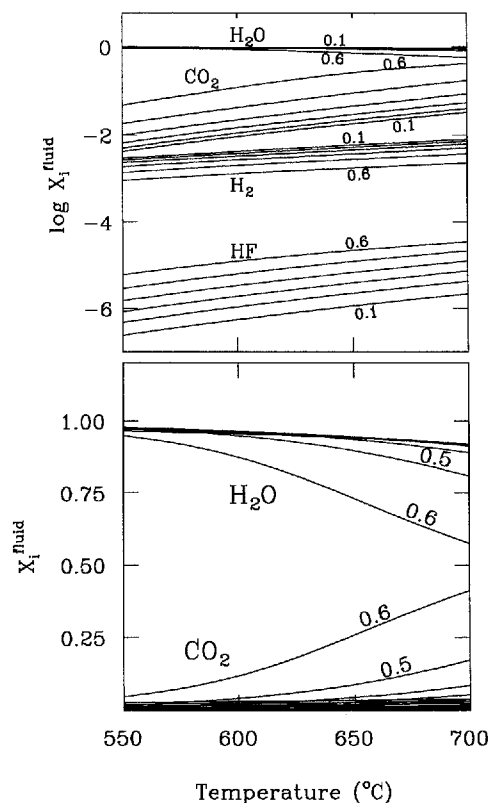


Fig. 5. Mole fractions of C–O–H–F fluid species defined by the assemblage Fo+Clh+Do+Cc+Gr as functions of temperature and  $X_F^{\text{chl}}$  (labels on contours) in both log and linear units

(1982) from graphitic fluorphlogopite-bearing marbles from the Grenville Orogenic belt. Valley et al. argued that addition of F from an external reservoir was not required to account for the F-rich phases in the Grenville marbles, suggesting that fugacities of HF recorded by the xenolith marble may be intrinsic to impure dolostones metamorphosed at high temperatures.

## Oxygen and carbon isotopes

### Analytical methods

Carbon and oxygen isotopic compositions of carbonates were determined for  $\text{CO}_2$  extracted from 20 mg splits of powdered calcite and ~2 g whole-rock powders of skarn using the method of McCrea (1950).  $\text{CO}_2$  was extracted at 25 °C by reaction with 103%  $\text{H}_3\text{PO}_4$  (specific gravity=1.90) prepared according to the method described by Wachter and Hayes (1985). Reaction time was 8 hours. Dolomite was detected with the electron microprobe and in XRD powder diffraction patterns but staining procedures confirmed that its abundance is negligible relative to calcite in all of the marbles, thus no effort was made to separate the carbonates. Isotopic compositions were measured on a VG PRISM gas-ratio mass spectrometer at the University of Southern California. Oxygen isotope values are reported in standard per mil ( $\delta$ ) notation relative to V-SMOW (Vienna Standard Mean Ocean Water). Carbon isotope values are reported relative to V-PDB (Vienna Pee Dee Belemnite).

Silicate oxygen isotope ratio determinations were made on two 15 mg splits of diorite whole-rock powder at Purdue University. Oxygen was extracted by reaction with  $\text{BrF}_3$  in sealed Ni reaction vessels at 560 °C using a modification of the method described

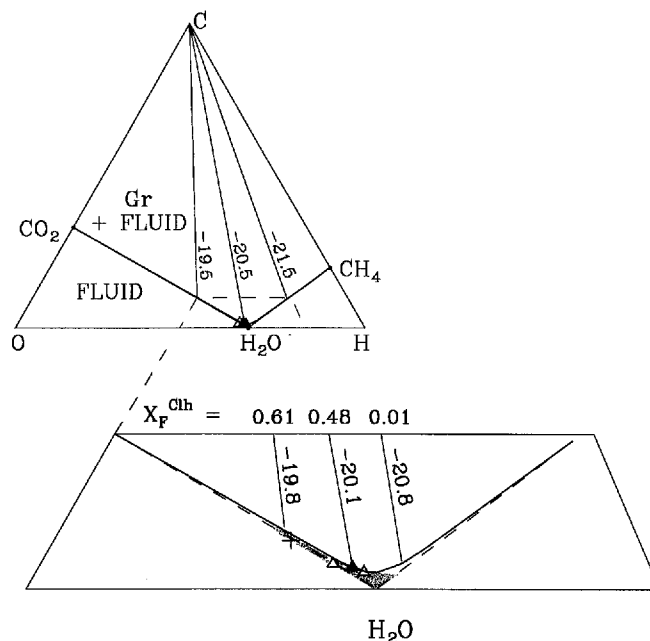


Fig. 6. C–O–H representation of the graphite-saturation surface at 600 °C and 6 kb, projections of the C–O–H–F equilibrium fluid composition defined by sample GM–90–11 (solid triangle, graphite present), and projected fluid compositions defined by samples GM–90–2 and GM–90–1 (open triangles, graphite absent). Gr+fluid tie lines are labeled with  $\log f_{\text{O}_2}$ . Patterned region in the enlargement shows the model infiltrated fluid compositions consistent with inequalities (7) and (8) given in the text based on a range of  $X_F^{\text{chl}}$  from 0.00 to 0.61. The cross symbol shows the infiltrated fluid composition which is consistent with both the inequality constraints and the  $\delta^{18}\text{O}_{\text{Cc}}$  and  $\delta^{13}\text{C}_{\text{Cc}}$  data. Tie lines in the enlargement are labeled with both  $\log f_{\text{O}_2}$  and corresponding  $X_F^{\text{chl}}$

by Clayton and Mayeda (1963). Replicate analyses of NBS–28 quartz standard yielded a mean  $\delta^{18}\text{O}_{\text{V-SMOW}}$  of  $9.7 \pm 0.2\text{‰}$ .

## Results

The oxygen and carbon isotopic compositions of calcite in the interior of the xenolith are slightly lower than many unmetamorphosed carbonates (Table 5). The extent of  $^{18}\text{O}$  depletion relative to unmetamorphosed dolostones cannot be constrained because of the lack of protolith rocks in the region. Variations in  $\delta^{18}\text{O}_{\text{Cc}}$  persist on a cm scale in the xenolith interior as shown by dental-drill sampling of GM–90–11. A relatively pure white Cc layer adjacent to a Clh-rich layer (layers are approximately 1 cm in thickness) is depleted in  $\delta^{18}\text{O}$  by 0.8‰ relative to surrounding dark gray Cc in more silicate-rich zones (cf. 18.7 and 19.5‰, respectively).

Both  $\delta^{18}\text{O}$  and  $\delta^{13}\text{C}$  in marble Cc exhibit systematic depletions adjacent to contacts with endoskarn relative to the interior of the xenolith. Values of  $\delta^{18}\text{O}_{\text{Cc}}$  decrease from a maximum of 19.5 near the xenolith center to 12.6 within less than a meter of endoskarn contacts (Fig. 2).  $\delta^{13}\text{C}_{\text{Cc}}$  shows a similar sympathetic depletion from 3.0 to 1.4‰.

Interstitial Cc comprises 1.3 wt.% of the outer skarn bulk rock and yields  $\delta^{18}\text{O}_{\text{Cc}}$  of 7.5 and  $\delta^{13}\text{C}_{\text{Cc}}$  of –2.9.

**Table 5.** Carbon and oxygen isotope data for marble calcite, skarn calcite, and diorite whole-rock<sup>a</sup>

Sample	$\delta^{18}\text{O}_{\text{V-SMOW}}$	$\delta^{13}\text{C}_{\text{V-PDB}}$	Description
GM-90-1	18.4	2.4	Average marble calcite
GM-90-2	14.3	1.4	Average marble calcite
GM-90-7	12.6	1.7	Average marble calcite
GM-90-10	16.1	2.1	Average marble calcite
GM-90-11	18.7	2.9	Average marble calcite
GM-90-11-1	19.3	2.9	Light gray calcite
GM-90-11-2	19.3	2.9	Light gray calcite
GM-90-11-3	18.7	3.0	White calcite
GM-90-11-4	19.5	3.0	Dark gray calcite in Clh-rich layer
GM-90-11-5	19.4	2.9	Dark gray calcite in Fo-rich layer
GM-90-11-6	19.5	2.9	Dark gray calcite in Fo-rich layer
GM-90-11-7	19.5	2.4	Dark gray calcite in Clh-rich layer
GM-90-3	7.5	-2.9	Outer skarn calcite (1.3 wt%)
GM-90-6	23.1	-3.4	Inner skarn calcite (0.3 wt%)
GM-90-8	21.3	-3.1	Inner skarn calcite (0.4 wt%)
GM-90-4	7.1	-	Diorite whole-rock, margin of xenolith
GM-90-9	6.2	-	Diorite whole-rock, within inner skarn

<sup>a</sup> All values in per mil

These are the lowest isotopic values obtained from the xenolith and its environs (Fig. 2, Table 5). In contrast, the inner skarns yield only 0.3 to 0.4 wt.% interstitial Cc and their  $\delta^{18}\text{O}_{\text{Cc}}$  are higher than any values obtained from the xenolith (Table 5). Low Cc contents similar to those obtained from the inner skarns and high  $\delta^{18}\text{O}$  (up to 31.3) are characteristic of caliche carbonate cement extracted from other silicate rocks in the region as determined during this and other studies. We therefore consider the  $\text{CO}_2$  extracted from the inner skarns to have a significant caliche component. Accordingly, only the outer skarn Cc isotopic data are used for petrologic modeling later.

We interpret the depletions in Cc  $^{18}\text{O}$  and  $^{13}\text{C}$  near endoskarn contacts to be the result of infiltration of isotopically light skarn fluids into the surrounding xenolith marble. The ~1 cm white calcite layer adjacent to a Clh-bearing zone in the interior of the xenolith may be a centimeter-scale analog to these skarn-zone margins in that there is a spatial correlation between abundant Clh and heavy isotope depletion in Cc for both. In the fluid-dominated environments represented by the endoskarns, the isotopic composition of interstitial Cc would have been controlled by the isotopic composition of the skarn fluid in all probability. The outer endoskarn Cc is therefore used to constrain the isotopic composition of the skarn fluid in this study.

Oxygen extracted from a whole-rock sample of diorite collected less than 1 m from the outer skarn contact yields a  $\delta^{18}\text{O}$  of 7.1 (Table 5). The average  $\delta^{18}\text{O}$  for 7 unaltered whole-rock samples from several localities throughout the diorite pluton is  $7.2 \pm 0.2$  (Young et al. 1992), indicating that the diorite has been unaffected by isotopic exchange with the marble xenolith on the scale of 1 m.

#### Zero-dimensional isotope model

It is apparent from Fig. 4 that Clh at the margin of the marble xenolith grew by a reaction involving both decarbonation and fluid infiltration. The magnitudes of the isotopic shifts expected as a result of this reaction are demonstrated by applying the zero-dimensional numerical approach simulating combined Rayleigh distillation-infiltration described by Rumble (1982). Results of these numerical calculations for the case of infiltration of pure  $\text{H}_2\text{O}$  at the invariant point are shown as  $\delta^{18}\text{O}_{\text{Cc}}$  isopleths in Fig. 4. Since they both refer to pure  $\text{H}_2\text{O}$ , the volumetric fluid-rock ratio and  $\delta^{18}\text{O}_{\text{Cc}}$  isopleths in Fig. 4 are compatible and can be used to ascertain the isotopic shifts associated with a given accumulated volume of infiltrated fluid in the context of this box model. The isotopic composition of the infiltrated fluid used to construct the  $\delta^{18}\text{O}_{\text{Cc}}$  isopleths is constrained by Cc from the outer skarn based on the assumption that the volume of Cc was small relative to the fluid volume in the skarn zones. The outer skarn  $\delta^{18}\text{O}_{\text{Cc}}$  of 7.5 suggests an equilibrium  $\text{H}_2\text{O}$  fluid  $\delta^{18}\text{O}$  of 6.8 at the invariant point temperature of 600 °C (O'Neil et al. 1969). Other specific parameters used in these calculations are listed in Table 6.

The isotope ratio isopleths in Fig. 4 would suggest that the maximum possible shift in  $\delta^{18}\text{O}_{\text{Cc}}$  in the marble resulting from infiltration of pure  $\text{H}_2\text{O}$  ( $\delta^{18}\text{O} = 6.8$ ) during growth of Clh is approximately -2.0‰. The observed shift from the center of the xenolith (sample GM-90-11) to the margin (sample GM-90-2) is approximately -5.0‰ and the maximum shift from the center of the xenolith to any of the skarn contacts is -6.9‰. One commonly invoked explanation for such discrepancies is that significantly more water passed through the rock than was needed for reaction. Alternative explanations, as noted already with reference to Fig. 4, are that zero-dimensional modeling and the assumption of a pure  $\text{H}_2\text{O}$  infiltrating fluid are over-simpli-

**Table 6.** Example result of numerical simulation of progress of reaction 1 driven by H<sub>2</sub>O infiltration at 600 °C and 6 kbar<sup>a</sup>

Phase/species	$\delta^{18}\text{O}_i^b$	$\delta^{13}\text{C}_i^b$	oxygens <sub>i</sub> <sup>c</sup>	$\delta^{18}\text{O}_f^b$	$\delta^{13}\text{C}_f^b$	oxygens <sub>f</sub>
Calcite	19.4	3.0	62	17.6	3.0	63
Forsterite	15.1	—	13	13.3	—	13
Spinel	11.7	—	2.4	9.8	—	2.7
Dolomite	19.6	3.4	0.8	17.8	3.4	0.0
Chlorite	18.1	—	3.3	16.2	—	2.4
Clinohumite	18.1	—	0.8	16.2	—	1.5
CO <sub>2</sub>	12.1	0.5	( $2.8 \times 10^{-2}$ )	12.1	0.5	( $2.8 \times 10^{-2}$ )
H <sub>2</sub> O	6.5	—	(0.14)	6.5	—	(0.14)

<sup>a</sup> *i* = initial conditions of system; *f* = final conditions of system.

<sup>b</sup> Initial calcite  $\delta$  measured; others from fractionation factors of Bottinga (1968), Chiba et al. (1989), Clayton et al. (1972), O'Neil et al. (1969), and Sheppard and Schwarz (1970)

<sup>c</sup> Oxygen proportions reflect best estimate of mode of sample GM-90-11 from XRD and petrographic inspection

fications representing untenable circumstances. A model which overcomes these shortfalls, and in so doing explains both the net-transfer reaction history of the marble and the attendant isotopic shifts, is presented next. It involves more realistic fluid compositions and utilizes continuum mechanics to describe the transport of fluid.

### Composition and transport of the infiltrated fluid

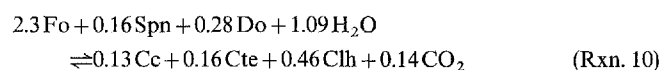
Pervasive interaction between the Granite Mountains xenolith and an external fluid requires that the fluid penetrated the marble along interconnected channels and that the scale of the channels was small in comparison to the size of the xenolith. The fluid cavities could have comprised connected grain edges if the solid-solid-fluid dihedral angle was less than 60° (Brenan 1991). Holness and Graham (1991) showed that this critical condition obtains in calcite at 650 °C and a pressure of 1 kb if the mole fraction of CO<sub>2</sub> in a mixed H<sub>2</sub>O-CO<sub>2</sub> pore fluid is greater than 0.2 and less than 0.6. Watson et al. (1990) showed that there is, in general, a negative correlation between dihedral angle and pressure, suggesting that the dihedral-angle minimum observed at 1 kb might expand to lower  $X_{\text{CO}_2}$  commensurate with Clh stability at the ca. 6 kb pressures estimated for the Granite Mountains. Alternatively, the interconnected fluid could have occupied an extensive network of microcracks. Presence of CO<sub>2</sub> in the crack-filling fluid would have inhibited healing (Brenan 1991). The time scales for persistence of microcrack-induced permeability can be on the order of 1 Ma at high temperatures (e.g., Hickman and Evans 1988).

To the extent that the fluid channels were uniformly distributed and small (micrometer scale), continuum mechanics can be applied to the marble system. Using the continuum concept, the record of net-transfer reaction progress provides critical constraints on the composition of the infiltrated fluid and a minimum estimate for the time-integrated fluid flux. The isotope data and the net-transfer reaction history in concert constrain the relative importance of advective and diffusive fluid transport in the marble as well as the infiltrated fluid composition.

It is convenient to reference the transport calculations to a single time interval for the metamorphic event. Calculations were made using a reference time of 1 Ma. This interval can be taken as an approximate upper limit based on studies of other contact metamorphic events (Kerrick et al. 1991).

### Infiltrated fluid composition

The net-transfer reaction history recorded by growth of Clh and loss of Gr is completely described by two linearly independent reactions:



Rxn. 10 represents the net Clh-producing reaction prescribed by the relative modes of samples GM-90-11, representing the unreacted interior of the xenolith, and GM-90-2, representing the reacted margin, as shown in Fig. 4. Rxn. 11 describes the breakdown of graphite and was not considered in Fig. 4 since the latter diagram was based on interaction with a binary CO<sub>2</sub>-H<sub>2</sub>O fluid only. The actual whole-rock reaction which occurred in the marble is a linear combination of Rxn. 10 and Rxn. 11. The relative contributions of the two component reactions to the overall reaction is dictated by their reaction progress variables,  $\xi_{10}$  and  $\xi_{11}$ . The amount of Clh produced (Fig. 4) suggests a maximum value of  $1.1 \times 10^{-3}$  mol cm<sup>-3</sup> for  $\xi_{10}$ . Assignment of a maximum  $\xi_{11}$  requires an estimate of the amount of Gr consumed. Judging from sample GM-90-11, the amount of graphite in the marble consumed by reaction was on the order of 0.5 vol.%, corresponding to a value of  $4.7 \times 10^{-4}$  mol cm<sup>-3</sup> for  $\xi_{11}$ . The efficacy with which Gr buffers fluid composition (cf. the stoichiometries of Rxn. 10 and Rxn. 11) necessitates explicit examination of the effects of variable amounts of Gr on the transport calculations where possible.

The observation that both Rxn. 10 and Rxn. 11 progressed in the positive direction (left to right as written)

towards the margin of the xenolith places one-sided limits on the composition of the infiltrated fluid. Spontaneous forward progress of reactions 10 and 11 under isothermal and isobaric conditions is expressed by the inequality (e.g., Guggenheim 1967):

$$\int_0^t \left[ \frac{\partial(\ln K)}{\partial \xi} \frac{d\xi}{dt'} \right] dt' > 0 \quad (4)$$

where the partial derivative refers to fixed  $P$  and  $T$ ,  $K$  and  $\xi$  represent the activity products and reaction progress variables for the respective reactions, and  $t$  is the time interval over which the reactions took place. Since the activities of the solid phases in these reactions were constant or nearly so (e.g., small variations in  $X_{\text{F}}^{\text{Ch}}$ , graphite was present during progress of Rxn. 11), inequality (4) applied to Rxn. 10 and Rxn. 11 results in the following two constraints on the system:

$$da_{\text{CO}_2} > 8 \left( \frac{a_{\text{CO}_2}}{a_{\text{H}_2\text{O}}} \right) da_{\text{H}_2\text{O}} \quad (5)$$

$$da_{\text{CH}_4} > 2 \left( \frac{a_{\text{CH}_4}}{a_{\text{H}_2\text{O}}} \right) da_{\text{H}_2\text{O}} - \left( \frac{a_{\text{CH}_4}}{a_{\text{CO}_2}} \right) da_{\text{CO}_2} \quad (6)$$

where inequality (5) is a requirement for growth of Clh and inequality (6) is a requirement for resorption of Gr. Spontaneous  $+\xi$  in this system was induced by loss of heat and by changes in fluid composition imposed by fluid infiltration (Fig. 4), requiring  $-\xi$  displacements from equilibrium by these two processes. Inequalities (5) and (6) therefore apply to changes in fluid composition brought about by infiltration if the inequality signs are reversed. The range of fluid compositions considered in this study is sufficiently small (i.e., near  $\text{H}_2\text{O}$  in Fig. 6) that activity coefficients for the fluid species are essentially constant. With the approximation of constant activity coefficients, multiplication of inequalities (5) and (6) by  $-1$  yields two inequality constraints on the changes in fluid composition which could have caused forward progress of Rxn. 10 and Rxn. 11:

$$dX_{\text{CO}_2}^{\text{In}} < 8 \left( \frac{X_{\text{CO}_2}}{X_{\text{H}_2\text{O}}} \right) dX_{\text{H}_2\text{O}}^{\text{In}} \quad (7)$$

$$dX_{\text{CH}_4}^{\text{In}} < 2 \left( \frac{X_{\text{CH}_4}}{X_{\text{H}_2\text{O}}} \right) dX_{\text{H}_2\text{O}}^{\text{In}} - \left( \frac{X_{\text{CH}_4}}{X_{\text{CO}_2}} \right) dX_{\text{CO}_2}^{\text{In}} \quad (8)$$

where the superscript  $^{\text{In}}$  denotes displacement from the equilibrium fluid composition caused by infiltration. Interpretation of inequalities (7) and (8) is straightforward. For example, (7) states that infiltration-driven growth of Clh could have occurred only if the fluid which entered the system caused a shift in  $X_{\text{H}_2\text{O}}$  greater than concomitant changes in  $X_{\text{CO}_2}$  by a factor of 8 ( $X_{\text{CO}_2}/X_{\text{H}_2\text{O}}$ ). This requirement is appropriate for the C–O–H–F or C–O–H fluid systems. It is less restrictive than the analogous condition in the  $\text{CO}_2$ – $\text{H}_2\text{O}$  fluid system because both  $X_{\text{CO}_2}$  and  $X_{\text{H}_2\text{O}}$  are permitted to increase

whereas in the binary system  $dX_{\text{CO}_2} = -dX_{\text{H}_2\text{O}}$  (e.g., Fig. 4).

Inequalities (7) and (8) delimit infiltrated fluid compositions which could have caused growth of Clh and consumption of Gr in the marble. For any positive displacement from an equilibrium fluid composition  $dX_{\text{H}_2\text{O}}^{\text{In}}$ , inequality (7) permits calculation of a maximum  $dX_{\text{CO}_2}^{\text{In}}$  subject to summing constraints on the mole fractions. Inequality (8) can be used to compute the corresponding maximum  $dX_{\text{CH}_4}^{\text{In}}$ . The maximum  $dX_{\text{H}_2\text{O}}^{\text{In}}$  corresponds to the limiting case where the infiltrated fluid was pure  $\text{H}_2\text{O}$ . In practice, two sets of model fluids for various  $dX_{\text{H}_2\text{O}}^{\text{In}}$  can be obtained as a result of the summing constraints on the mole fractions. One set is derived by taking the maximum  $X_{\text{CO}_2}^{\text{In}}$  and computing  $X_{\text{CH}_4}^{\text{In}}$  by difference (fluid species other than  $\text{H}_2\text{O}$ ,  $\text{CO}_2$ , and  $\text{CH}_4$  do not effectively enter into the summing constraints under these conditions). The other results from choosing the maximum  $X_{\text{CH}_4}^{\text{In}}$  and deriving  $X_{\text{CO}_2}^{\text{In}}$  by difference.

#### Estimate of minimum advective fluid flux

As shown by Baumgartner and Ferry (1991), the equation of continuity for  $\text{H}_2\text{O}$  in the marble, integrated over the time required for growth of Clh, can be written as:

$$\Delta n_{\text{H}_2\text{O}}^{\text{rxn}10} + \Delta n_{\text{H}_2\text{O}}^{\text{rxn}11} = \nabla \cdot (X_{\text{H}_2\text{O}} \mathbf{J}_m) \quad (9)$$

where  $\Delta n_{\text{H}_2\text{O}}^{\text{rxn}10}$  and  $\Delta n_{\text{H}_2\text{O}}^{\text{rxn}11}$  are the moles per unit rock volume of  $\text{H}_2\text{O}$  produced or consumed by Rxn. 10 and Rxn. 11 respectively, and  $\mathbf{J}_m$  is the time-integrated Darcy flux vector with scalar units of  $\text{mol}/\text{cm}^2$ . Implicit in Eq. (9) is a low porosity and predominance of advection of fluid over diffusive transport processes. We approximate the infiltration as being one-dimensional from the margin of the xenolith to its center. In this case, Eq. (9) reduces to:

$$J_m = \frac{\xi_{10}(v_{\text{H}_2\text{O},10} - X_{\text{H}_2\text{O}}(v_{\text{H}_2\text{O},10} + v_{\text{CO}_2,10} + v_{\text{CH}_4,10}))}{\left( \frac{dX_{\text{H}_2\text{O}}}{dz} \right)} + \frac{\xi_{11}(v_{\text{H}_2\text{O},11} - X_{\text{H}_2\text{O}}(v_{\text{H}_2\text{O},11} + v_{\text{CO}_2,11} + v_{\text{CH}_4,11}))}{\left( \frac{dX_{\text{H}_2\text{O}}}{dz} \right)} \quad (10)$$

where  $v_{i,j}$  are the stoichiometric coefficients for fluid species  $i$  in reaction  $j$  and  $z$  is the one-dimensional direction coordinate in cm. Equation (10) is analogous to Eq. 12 of Baumgartner and Ferry (1991), but differs from the latter in that the linearly independent components of the whole-rock reaction are explicitly treated,  $\text{CH}_4$  is included as a potentially important species in the fluid, and no assumptions regarding degree of attainment of equilibrium, necessary for expansion of the denominator in terms of  $T$  and  $P$  for example, have been made.

The minimum time-integrated flux of fluid which could have caused growth of Clh and consumption of

Gr is obtained from  $\xi_{10}$ ,  $\xi_{11}$ , and Eq. (10) by inserting the maximum  $dX_{\text{H}_2\text{O}}/dz$ . Assuming that there was a significant component of fluid flow from the margin to the center of the xenolith, the zone separating Clh-bearing marbles from Fo-bearing marbles can be regarded as being a smeared net-transfer reaction front. Fluid which entered the xenolith upstream of the reaction front retained its initial composition  $X_{\text{H}_2\text{O}}^{\text{In}}$ . Fluid which flowed downstream from the front was likely in local equilibrium with the marble (Bickle and Baker 1990; Baumgartner and Ferry 1991), and was characterized by  $X_{\text{H}_2\text{O}}^{\text{Eq}}$ . The minimum  $J_m$  is then constrained by maximum  $(X_{\text{H}_2\text{O}}^{\text{Eq}} - X_{\text{H}_2\text{O}}^{\text{In}})$  and the minimum distance over which this change from  $X_{\text{H}_2\text{O}}^{\text{In}}$  to  $X_{\text{H}_2\text{O}}^{\text{Eq}}$  occurred. Sampling in this study was such that the existence of at least partially unreacted rock at a distance as small as 50 cm from the outer skarn contact, i.e., a distance just beyond that of sample GM-90-1, cannot be precluded. Using 50 cm as the minimum  $dz$  and the maximum  $(X_{\text{H}_2\text{O}}^{\text{Eq}} - X_{\text{H}_2\text{O}}^{\text{In}})$  defined by  $X_{\text{H}_2\text{O}}^{\text{In}} = 1$  and  $X_{\text{H}_2\text{O}}^{\text{Eq}} = 0.955$  (Table 4), Eq. (10) yields:

$$J_m^{\text{min}} = 201 \xi_{10} + 2222 \xi_{11} \quad (11)$$

where it was shown above that  $\xi_{10}$  is on the order of  $1.1 \times 10^{-3} \text{ mol cm}^{-3} \text{ rock}$ . Equation (11) demonstrates that the calculated minimum time-integrated flux is markedly sensitive to estimates of the amount of Gr consumed during the whole-rock reaction. Figure 7 shows the calculated minimum flux as a function of both the volume per cent of Gr consumed and  $X_{\text{H}_2\text{O}}^{\text{Eq}}$  defined by variable  $X_{\text{F}}^{\text{Clh}}$ . For the range of measured  $X_{\text{F}}^{\text{Clh}}$  and estimated original vol. % of Gr of 0.5%, the minimum time-

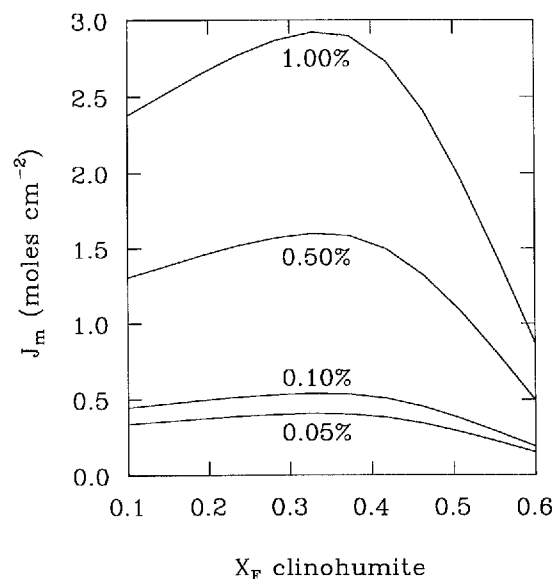


**Fig. 7.** Minimum time-integrated fluid flux responsible for growth of Clh as a function of volume per cent graphite consumed by reaction (labels on contours) and  $X_{\text{F}}^{\text{Clh}}$ . Curves were calculated from Eq. (10). Note the strong dependence of the estimated integrated flux on the amount of graphite consumed

integrated fluid flux is approximately  $1 \text{ mol fluid/cm}^2$ , or  $22 \text{ cm}^3/\text{cm}^2$ . The corresponding minimum Darcy flux based on a reference time of 1 Ma is  $7.0 \times 10^{-13} \text{ cm}^3/\text{cm}^2 \text{ sec}$ .

#### Estimate of maximum advective fluid flux

In the absence of diffusive and dispersive transport mechanisms (the effects of kinetic barriers to isotope exchange, ignored for the present, are discussed later), the tenets of mass transport theories predict that  $\delta^{18}\text{O}_{\text{Cc}}$  and  $\delta^{13}\text{C}_{\text{Cc}}$  are unlikely to covary as a result of fluid infiltration (Bickle and McKenzie 1987; Baumgartner and Rumble 1988; Blattner and Lasseby 1990). This is because the isotope exchange fronts for oxygen and carbon would then be infinitely sharp, and because the fronts will occur in general at different positions along a rock column owing to different solid-fluid distribution properties. Covariation due to infiltration requires "smearing" of the isotope exchange fronts by diffusive-dispersive processes, and requires that the distance between centroids of the  $\delta^{18}\text{O}_{\text{Cc}}$  and  $\delta^{13}\text{C}_{\text{Cc}}$  exchange fronts not exceed the characteristic length scale of effective isotope diffusion-dispersion. The ceiling on the spacing of the  $\delta^{18}\text{O}_{\text{Cc}}$  and  $\delta^{13}\text{C}_{\text{Cc}}$  fronts in turn limits the time-integrated advective flux through the relation (Baumgartner and Rumble 1988):

$$J_m^{\text{max}} = \frac{z^{\delta^{18}\text{O}} - z^{\delta^{13}\text{C}}}{(1/K_d^{18\text{O}} - 1/K_d^{13\text{C}}) \hat{V}_{\text{fluid}}^{P,T}} \quad (12)$$

where  $z^{\delta^{18}\text{O}}$  and  $z^{\delta^{13}\text{C}}$  are the relative positions of the centroids of the isotope fronts,  $K_d^{18\text{O}}$  and  $K_d^{13\text{C}}$  are the solid-fluid distribution coefficients for the indicated isotopes as defined by Baumgartner and Rumble (1988), and  $\hat{V}_{\text{fluid}}^{P,T}$  is the molar volume of the fluid at  $P$  and  $T$ .

The combined effective diffusion-dispersion coefficient for the marble is taken as  $D_{\text{eff}} = \beta D_{\text{diff}} + D_{\text{disp}}$  where  $\beta$  is the interconnected porosity,  $D_{\text{diff}}$  is the diffusion coefficient of oxygen or carbon in the fluid, and  $D_{\text{disp}}$  is the hydrodynamic dispersion coefficient. An appropriate value for  $D_{\text{diff}}$  is  $1.0 \times 10^{-4} \text{ cm}^2 \text{ sec}^{-1}$  (Bickle and McKenzie 1987; Labotka 1991). Diffusion calculations using this  $D_{\text{diff}}$  show that Cc with undepleted  $\delta^{13}\text{C}$  and  $\delta^{18}\text{O}$  near the margin of the xenolith (sample GM-90-1) requires an interconnected porosity of  $\sim 1.0 \times 10^{-4}$  or less for  $t$  approaching 1 Ma. Shorter times permit larger porosities but the characteristic length scale of diffusion would be unchanged. Neglecting the uncertain  $D_{\text{disp}}$ , the implied characteristic diffusion length  $(D_{\text{eff}} t)^{1/2}$  is 560 cm for  $t = 1 \text{ Ma}$ . The  $(D_{\text{eff}} t)^{1/2}$  together with distribution coefficients appropriate for  $\text{H}_2\text{O}$ -rich fluid compositions in this study yield a maximum  $J_m$  of approximately  $93 \text{ mol/cm}^2$ , corresponding to a Darcy flux of  $6.5 \times 10^{-11} \text{ cm}^3/\text{cm}^2 \text{ sec}$  for a period of 1 Ma. An advective fluid flux significantly greater than this can not explain covariation between  $\delta^{18}\text{O}_{\text{Cc}}$  and  $\delta^{13}\text{C}_{\text{Cc}}$ .

### Transport model

A one-dimensional fluid transport model was called upon to explain the proximity of the  $\delta^{18}\text{O}_{\text{Cc}}$  and  $\delta^{13}\text{C}_{\text{Cc}}$  depletions to the outer skarn, the fact that the Clh-producing reaction was displaced further into the xenolith than the isotope fronts, and the curvature defined by the data in  $\delta^{18}\text{O}_{\text{Cc}} - \delta^{13}\text{C}_{\text{Cc}}$  space. Fluid was assumed to originate from the outer skarn and flow was from the margin to the interior of the xenolith in these calculations. Multiple skarn zones were not considered.

For the isotopes, the model consists of solutions to the equations of continuity for  $^{18}\text{O}$  and  $^{13}\text{C}$  in rock experiencing both advective and diffusive fluid infiltration and instantaneous isotopic exchange between solid and fluid. The solution to these equations for the boundary condition of constant  $\delta^{18}\text{O}$  and  $\delta^{13}\text{C}$  at the entrance to the one-dimensional flow path is given by Blattner and Lassey (1990) as:

$$\delta_{\text{sol}}^i(z, t) = \delta_{\text{sol}}^{i0} + (\Delta_{\text{sol-f}} + \delta_{\text{fl}}^i - \delta_{\text{sol}}^{i0}) \cdot \left[ \frac{1}{2} \operatorname{erfc} \left( \frac{z - \left( \frac{Jt}{\beta + (1-\beta) K_d^i} \right)}{2((D_{\text{eff}}/(\beta + (1-\beta) K_d^i)) t)^{1/2}} \right) + \frac{1}{2} \exp \left( \frac{Jz}{D_{\text{eff}}} \right) \operatorname{erfc} \left( \frac{z + \left( \frac{Jt}{\beta + (1-\beta) K_d^i} \right)}{2((D_{\text{eff}}/(\beta + (1-\beta) K_d^i)) t)^{1/2}} \right) \right] \quad (13)$$

where  $i$  represents  $^{18}\text{O}$  or  $^{13}\text{C}$ ,  $\delta_{\text{sol}}^{i0}$  and  $\delta_{\text{sol}}^i(z, t)$  are the initial and final isotopic compositions of the bulk solid rock, respectively,  $\delta_{\text{fl}}^{i0}$  is the initial isotopic composition of the infiltrating fluid, and  $\Delta_{\text{sol-f}}$  is the equilibrium per mil fractionation between solid and fluid. Initial fluid  $\delta^{18}\text{O}$  and  $\delta^{13}\text{C}$  were derived from the outer skarn Cc as described already.

The fluid-driven net-transfer reaction front, representing the change from reactants to products in Rxn. 10 and Rxn. 11 in the marble, was modeled as an abrupt discontinuity in mineralogy propagated at a velocity

$$v_{\text{rxn}} = \frac{J^0 (X_{\text{H}_2\text{O}}^{\text{Eq}} - X_{\text{H}_2\text{O}}^{\text{In}})}{\xi_{\text{wr}} (v_{\text{H}_2\text{O}} - X_{\text{H}_2\text{O}} (v_{\text{H}_2\text{O}} + v_{\text{CO}_2\text{O}} + v_{\text{Clh}})) (1 - \phi^0)} \quad (14)$$

where  $J^0$  is the initial Darcy flux upstream of the reaction front,  $\phi^0$  is the total porosity of the unreacted rock downstream of the reaction front, and  $\xi_{\text{wr}}$  is the whole-rock reaction progress variable. Equation (14) is equivalent to velocity given by Bickle and Baker (1990, Eq. 5) for small porosities. There is a stable-isotope fractionation across the reaction front as well as changes in properties which affect  $\delta_{\text{sol}}^i(z, t)$  from Eq. (13). The effects of variations in the relative velocities of fluid-driven net-transfer reaction fronts and stable-isotope fronts were described by Bickle and Baker (1990). In this study,  $v_{\text{rxn}}$  proved to be greater than the velocities of the isotope fronts.

Model fluid compositions were derived by applying inequalities (7) and (8) to equilibrium fluids defined by  $X_{\text{F}}^{\text{Ch}}$  ranging from 0.00 to 0.61. The resulting potential

infiltrated fluid compositions are plotted in Fig. 6. The fluid fluxes in the model calculations were constrained to be between the maximum and minimum prescribed by Eq. (10) and (12). In addition to fluid composition and flux, the  $\delta^{18}\text{O}_{\text{Cc}} - \delta^{13}\text{C}_{\text{Cc}}$  trend is influenced by the relative values of the effective diffusion-dispersion coefficients for  $^{18}\text{O}$  and  $^{13}\text{C}$ . We assumed equal  $D_{\text{diff}}$  and equal  $D_{\text{eff}}$  for  $^{18}\text{O}$  and  $^{13}\text{C}$  in the calculations following. Equivalency of the diffusivities is a limiting case since application of the Stokes-Einstein equation to the relative radii of  $\text{H}_2\text{O}$  and  $\text{CO}_2$  molecules suggests that if the  $D_{\text{diff}}$  are unequal,  $D_{\text{diff}}^{13\text{C}} < D_{\text{diff}}^{18\text{O}}$ .

For equal diffusivities in the fluid, the model calculations show that the  $\delta^{18}\text{O}_{\text{Cc}} - \delta^{13}\text{C}_{\text{Cc}}$  trend requires an infiltrating fluid with  $X_{\text{CO}_2}^{\text{In}}$  no lower than 0.095. Although the data constrain the flux (see later),  $X_{\text{CO}_2}^{\text{In}}$  lower than this cannot explain the Cc isotope data irrespective of flux. The  $X_{\text{CO}_2}^{\text{In}}$  of 0.095 is consistent with inequalities (7) and (8) only if the equilibrium fluid is that corresponding to  $X_{\text{F}}^{\text{Ch}} = 0.60$  (proximity of the fluid with  $X_{\text{CO}_2}^{\text{In}} = 0.095$  to the equilibrium composition implied by  $X_{\text{F}}^{\text{Ch}} = 0.60$  in Fig. 6 is a reflection of this association). This  $X_{\text{F}}^{\text{Ch}}$  is approximately 0.1 greater than the average Clh composition for the xenolith. Since greater  $X_{\text{CO}_2}^{\text{In}}$  would imply still greater  $X_{\text{F}}^{\text{Ch}}$ , which would be further removed from the observed fluorine concentrations in Clh, the infiltrated fluid composition which is nearest to being consistent with both the isotope data and the

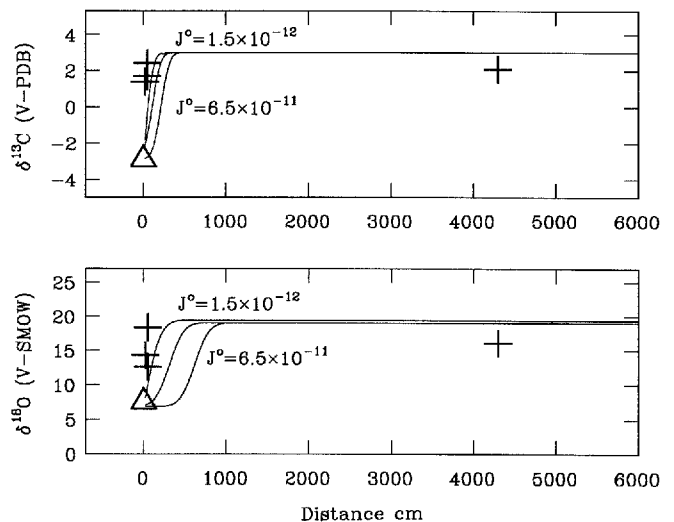


**Fig. 8.**  $\delta^{18}\text{O}_{\text{Cc}}$  and  $\delta^{13}\text{C}_{\text{Cc}}$  versus distance plots for the advective-dispersive fluid transport model described in the text and summarized in Table 7. Model curves are shown for the maximum and minimum advective fluid fluxes (in  $\text{cm}^3/\text{cm}^2 \text{ sec}$ , referenced to  $t = 1 \text{ Ma}$ ) derived in the text, and for their median. Discontinuities in the model curves result from isotope fractionations across the net-transfer reaction front and mark the location of the front for the respective fluxes. Also shown are representative xenolith Cc isotope data (crosses). The abscissa values indicate minimum distances from the nearest skarn zone for ease of comparison with the model. The triangle represents the outer skarn Cc isotope data used to define the infiltrated fluid isotopic composition. Note that the spatial distribution of the data are consistent with the minimum flux curve. Sizes of symbols reflect probable uncertainties (e.g., porosity) in model calculations, and not analytical uncertainties.

Clh chemistry is one with the minimum  $X_{\text{CO}_2}^{\text{In}}$  of 0.095. The maximum  $X_{\text{CH}_4}$  consistent with inequalities (7) and (8) yields insufficient carbon to affect the required shifts in  $\delta^{13}\text{C}_{\text{Cc}}$  despite large  $^{13}\text{C}$  equilibrium fractionation between Cc and  $\text{CH}_4$  (Fig. 6).

Transport model curves which incorporate the preferred infiltrated fluid composition shown in Fig. 6 are shown in Figs. 8 and 9 and summarized in Table 7. The curves span the permissible range in advective fluid flux. The minimum flux for the preferred fluid composition allowed by Eq. (10),  $44 \text{ cm}^3/\text{cm}^2$ , or  $1.4 \times 10^{-12} \text{ cm}^3/\text{cm}^2 \text{ sec}$  for  $t = 1 \text{ Ma}$ , is required to explain the isotope data (Fig. 8, Fig. 9). This is the flux downstream of the reaction front. There is an 8.3% decrease in flux with downstream flow across the reaction front, so that the minimum upstream flux is  $1.5 \times 10^{-12}$ .

The minimum flux places the model net-transfer reaction front 225 cm inward from the margin of the xenolith upon termination at  $t$ . Larger fluxes push the reaction front further into the interior of the xenolith (Fig. 8, Table 7), which is consistent with the occurrence of marble in which Fo is only partially replaced by Clh (sample GM-90-10) 40 m from the nearest skarn zone (Fig. 2), but they can not explain the simultaneous depletions in  $\delta^{18}\text{O}_{\text{Cc}}$  and  $\delta^{13}\text{C}_{\text{Cc}}$  (Fig. 9). The resolution of sampling, probable smearing of the net-transfer reaction front, and use of a unidirectional flow model preclude attaching greater significance to the predicted net-transfer reaction front location beyond noting that it lies further downstream than the model isotope fronts, which is consistent with observation.

The discrepancy between the observed average  $X_{\text{F}}^{\text{Clh}}$  of 0.51 and the model value of 0.60 can be explained

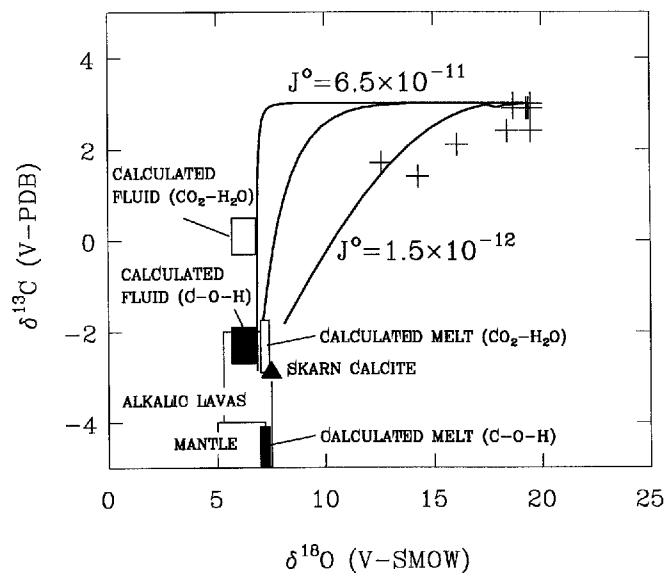


**Fig. 9.**  $\delta^{18}\text{O}$  versus  $\delta^{13}\text{C}$  plot comparing xenolith Cc data (crosses), outer skarn Cc (triangle), and fluid transport model curves shown in Fig. 8. Note that the covariation between  $\delta^{13}\text{C}_{\text{Cc}}$  and  $\delta^{18}\text{O}_{\text{Cc}}$  for the xenolith requires the minimum flux derived in the text. Also shown are calculated fields for skarn fluid and diorite melt based on maximum  $X_{\text{CH}_4}^{\text{Cc}}$  (C-O-H, solid boxes) and  $X_{\text{CH}_4}^{\text{Cc}} = 0$  ( $\text{CO}_2\text{-H}_2\text{O}$ , open boxes) in the fluid as discussed in the text. Fields for mantle and alkalic lavas are literature compilations

**Table 7.** Parameters for fluid transport models shown in Figs. 8 and 9

$X_{\text{F}}^{\text{Clh}}$	0.600
$X_{\text{CO}_2}^{\text{Eq}}$	0.119
$X_{\text{CH}_4}^{\text{Eq}}$	0.004
$X_{\text{CO}_2}^{\text{In}}$	0.095
$X_{\text{CH}_4}^{\text{In}}$	0.000
$\beta$	$1.0 \times 10^{-4}$
$D_{\text{diff}}^{\text{a}}$	$1.0 \times 10^{-4} \text{ cm}^2 \text{ sec}^{-1}$
Temperature <sup>b</sup>	600 °C
$K_{\text{d}_{\text{upstream}}}^{18\text{O}}$ <sup>c</sup>	3.302
$K_{\text{d}_{\text{downstream}}}^{18\text{O}}$ <sup>d</sup>	2.961
$K_{\text{d}_{\text{upstream}}}^{13\text{C}}$ <sup>c</sup>	9.495
$K_{\text{d}_{\text{downstream}}}^{13\text{C}}$ <sup>d</sup>	6.797
Duration $t$	1 Ma
$Z_{\text{F}}^{\text{rxnfront}} = 1.5 \times 10^{-12} \text{ cm}^3/\text{cm}^2\text{sec}$ <sup>e</sup>	225 cm
$Z_{\text{F}}^{\text{rxnfront}} = 3.3 \times 10^{-11} \text{ cm}^3/\text{cm}^2\text{sec}$ <sup>e</sup>	4959 cm
$Z_{\text{F}}^{\text{rxnfront}} = 6.5 \times 10^{-11} \text{ cm}^3/\text{cm}^2\text{sec}$ <sup>e</sup>	9768 cm

<sup>a</sup> Diffusion coefficient in the fluid for both oxygen and carbon

<sup>b</sup> 600 °C equilibrium isotope fractionation factors taken from references in Table 5

<sup>c</sup> Solid-fluid distribution coefficients upstream of the net-transfer reaction front where solid = product minerals

<sup>d</sup> Solid-fluid distribution coefficients downstream of net-transfer reaction front where solid = reactant minerals

<sup>e</sup> Position of the net-transfer reaction front for the specified upstream fluid flux  $J^0$

by uncertainties in the thermochemical and activity-composition relations of Duffy and Greenwood (1979) (see Rice 1980 for a discussion). Alternatively, a model which meets all of the requirements described above can be calculated using the average observed  $X_{\text{F}}^{\text{Clh}}$  by raising  $D_{\text{diff}}^{13\text{C}}$  by a factor of ca. 2 relative to  $D_{\text{diff}}^{18\text{O}}$ . A higher diffusivity for  $^{13}\text{C}$  relative to  $^{18}\text{O}$  in the fluid is considered unlikely (see earlier). However, apparent effective diffusivities in the rock column could be indicative of isotope exchange kinetic factors which were not considered in these calculations. Significant kinetic barriers to exchange will smear isotope fronts such that the relative roles of kinetics and diffusive-dispersive transport are obscured (Blattner and Lassey 1990).

### Origin of infiltrated fluid

The deep crustal level of the Granite Mountains terrane during Jurassic time is inconsistent with infiltration of meteoric fluid. Based on apparent depth, it is more probable that the marble xenolith was invaded by fluids evolved by crystallizing diorite.

The equilibrium C-O-H-F fluid calculations suggest two scenarios for testing the hypothesis that the endoskarn  $\delta^{13}\text{C}_{\text{Cc}}$  derives from magmatic carbon. The difference between them lies with the role of reduced carbon. In the first scenario the fluid contains values near the maximum possible  $\text{CH}_4$  (Fig. 6). Substantial buffering by the graphitic marble during protracted fluid-

rock interaction is one possible source for the  $\text{CH}_4$ . For  $X_{\text{F}}^{\text{Ch}}$  of approximately 0.5 at 600 °C, the equilibrium  $X_{\text{CH}_4}^{\text{C}}$  is 0.14 and the maximum  $X_{\text{CH}_4}^{\text{C}}$  consistent with inequality (8) is 0.27. Using a conservative value of 0.20, equilibrium between skarn Cc and fluid at 600 °C dictates  $\delta^{13}\text{C}$  of  $-0.3$  and  $-12.3$  for  $\text{CO}_2$  and  $\text{CH}_4$ , respectively, and a fluid total carbon  $\delta^{13}\text{C}$  of  $-2.7$  (Bottinga 1969). If we further consider that the fluid carbon released by the dioritic magma was originally oxidized (e.g., Matthey et al. 1990), then the calculated  $\delta^{13}\text{C}$  for the melt is  $-5.1$  (Fig. 9). Petrologic studies of the diorite suggest that it represents an alkaline mantle-derived magma (Young et al. 1992). The magmatic  $\delta^{13}\text{C}$  in the buffered-fluid scenario is within the range expected for mantle carbon and other alkaline mafic magmas (Fig. 9; Pinneau and Javoy 1983; Taylor 1986).

In the second scenario, the infiltrated fluid remains oxidized with all carbon in the form of  $\text{CO}_2$  (or apparent  $\text{H}_2\text{CO}_3$ ). Since the carbon isotope fractionation between Cc and  $\text{CO}_2$  at 600 °C is similar to the fractionation between mafic melt and  $\text{CO}_2$  at near-solidus temperatures (Bottinga 1968; Chacko et al. 1989; Matthey et al. 1990), the skarn  $\delta^{13}\text{C}_{\text{Cc}}$  differs from the calculated magmatic  $\delta^{13}\text{C}$  by only 0.2‰ or less. The magmatic  $\delta^{13}\text{C}$  calculated for this case is anomalously high relative to nominal mantle values and is at the upper extreme of the alkali mafic lava range (Fig. 9).

The fluid  $\delta^{18}\text{O}$  calculated from skarn  $\delta^{18}\text{O}_{\text{Cc}}$  data permit a magmatic origin in view of existing fractionation factor data. The low  $\delta^{18}\text{O}_{\text{Cc}}$  of the outer skarn suggests a fluid  $\delta^{18}\text{O}$  of 6.8 using equilibrium fractionation between Cc and  $\text{H}_2\text{O}$ -dominated fluid at 600 °C. Moderately altered Pl from a diorite sample collected near the xenolith indicates a similar  $\delta^{18}\text{O}$  of 6.5 for an  $\text{H}_2\text{O}$ -rich fluid equilibrated at 600 °C (Young et al. 1991; Matsuhisa et al. 1979). Agreement between these independently-derived values supports the inferred fluid  $\delta^{18}\text{O}$ . Oxygen isotopic fractionation factors between silicate melts at near-solidus conditions and aqueous fluids are not well known. Experiments by Shettel (1978), as summarized by Ohmoto (1986), suggest  $\Delta_{\text{melt-H}_2\text{O}}$  values ( $\delta^{18}\text{O}_{\text{melt}} - \delta^{18}\text{O}_{\text{H}_2\text{O}}$ ) of between  $-2$  to  $+5$ ‰ depending on the composition of the melt. For this reason, the observed range in unaltered whole-rock  $\delta^{18}\text{O}$  (Young et al. 1992; Table 5) was used to define the magmatic  $\delta^{18}\text{O}$  in Fig. 9.

## Conclusions

The marble xenolith from the mid-crustal Granite Mountains plutonic complex exhibits mineralogical and stable isotopic evidence for fluid-rock interaction concentrated at its contacts with endoskarn zones. Analysis of the infiltration-driven net-transfer reaction, which involved growth of clinohumite and consumption of graphite, results in quantitative inequality constraints on the C–O–H–F composition of the infiltrated fluid. Models for the infiltration event are constrained by these inequalities, the measured  $\delta^{18}\text{O}_{\text{Cc}}$  and  $\delta^{13}\text{C}_{\text{Cc}}$  depletions, and the spatial relationships between the depletions in  $^{18}\text{O}$  and  $^{13}\text{C}$  in calcite and the occurrence of clinohumite.

The data are explained by infiltration of an aqueous fluid with a one-dimensional time-integrated advective flux of  $44 \text{ cm}^3/\text{cm}^2$  together with diffusive transport through fluid occupying an interconnected porosity of approximately  $1.0 \times 10^{-4}$  or less. Explicit formulation of the time-integrated flux equations in terms of the contribution of graphite consumption illustrates the efficacy of graphite as a buffer of  $\text{H}_2\text{O}$ -rich fluids and its importance as a potential indicator of fluid flux.

Mineral equilibria and the direction of progress of the clinohumite-producing reaction limit the possible concentrations of  $\text{CH}_4$  in the infiltrated fluid, but the range is sufficient to impart an uncertainty of approximately 2.0 per mil in the calculated  $\delta^{13}\text{C}$  of the fluid. In view of this uncertainty, the isotopic signature of the skarn calcite is compatible with a magmatic origin for the infiltrated fluid in this deep crustal terrane.

**Acknowledgements.** This research was supported by funds provided by the University of Southern California and NSF grants EAR-8904062 and -9105924 to J.M. During completion of this work the senior author was supported by a postdoctoral fellowship from the Geophysical Laboratory of the Carnegie Institution of Washington. We wish to thank Bob Jones for his help in using the UCLA electron microprobe facility, Eric Bender for performing XRF analyses, and J. Michael Palin and James M. Brenan for lively discussions. The investigations of the Granite Mountains plutonic complex were initiated on the suggestion of Keith A. Howard of the USGS, Menlo Park. We thank Jack M. Rice, Daniel Barnett, and John M. Ferry for constructive reviews which resulted in significant improvements over the original manuscript.

## Appendix

List of symbols, definitions, and mineral formulas

Cc	$(\text{Ca}, \text{Mg})\text{CO}_3$
Clh	$4\text{Mg}_2\text{SiO}_4 \cdot \text{Mg}_{1-x}\text{Ti}_x(\text{OH}, \text{F})_{2-2x}\text{O}_{2x}$
Cte	$\text{Mg}_5\text{Al}_2\text{Si}_3\text{O}_{10}(\text{OH})_8$
Do	$(\text{Ca}, \text{Mg})\text{CO}_3$
Fo	$\text{Mg}_2\text{SiO}_4$
Gr	C (graphite)
Spn	$\text{MgAl}_2\text{O}_4$
$\xi_i$	reaction progress, moles $\text{cm}^{-3}$
$\nu_{i,j}$	stoichiometric coefficient for species $i$ in reaction $j$
$\Delta n_{\text{H}_2\text{O}}^{\text{rxn}i}$	time-integrated molar production rate of $\text{H}_2\text{O}$ by reaction $i$ , moles $\text{cm}^{-3}$
Q	isobaric change in enthalpy, $\text{kJ}/\text{cm}^3$
$X_i^{\text{Eq}}$	mole fraction of component $i$ in fluid in equilibrium with rock
$X_i^{\text{In}}$	mole fraction of component $i$ in the infiltration fluid
$X_{\text{CH}_4}^{\text{C}}$	carbon fraction of $\text{CH}_4$ in fluid
$\Delta_{i-j}$	equilibrium isotope fractionation between phases $i$ and $j$ expressed as $\delta_i - \delta_j$
$\alpha_{i-j}$	equilibrium isotope fractionation factor for phases $i$ and $j$
$\delta_{\text{so}}^i(z, t)$	bulk solid isotopic composition (per mil) at time $t$ and position $z$
$\beta$	interconnected porosity
$\phi^0$	total porosity downstream of the net-transfer reaction front
$D_{\text{diff}}$	diffusion coefficient in fluid, $\text{cm}^2 \text{ sec}^{-1}$
$D_{\text{disp}}$	hydrodynamic dispersion coefficient, $\text{cm}^2 \text{ sec}^{-1}$
$D_{\text{eff}}$	effective diffusion coefficient in a porous medium, $\beta D_{\text{diff}} + D_{\text{disp}}$
$N_j$	total moles of oxygen or carbon per mole of phase $j$

$K_d^i$	$(N_{\text{solid}}/N_{\text{fluid}})_{\text{fluid-solid}}$ for the specified carbon or oxygen isotope $i$
$t$	duration of infiltration event, sec
$J_m$	time-integrated molar fluid flux vector
$J_m$	one-dimensional time-integrated molar fluid flux, moles/cm <sup>2</sup>
$J$	one-dimensional Darcy fluid flux, cm <sup>3</sup> /cm <sup>2</sup> sec
$J^0$	one-dimensional Darcy fluid flux upstream of the net-transfer reaction front, cm <sup>3</sup> /cm <sup>2</sup> sec
$v_{\text{rxn}}$	velocity of net-transfer reaction front, cm sec <sup>-1</sup>
$z$	one-dimensional distance coordinate, cm
$z^i$	distance of centroid of front $i$ from an upstream fluid source, cm

## References

- Anderson JL, Barth AP, Young ED, Davis MJ, Farber D, Hayes EM, Johnson KA (1989) Plutonism across the Tujung-North American terrane boundary: a middle to upper crustal view of two juxtaposed arcs. In: Bartholomew MJ (ed) Proceedings of the 8th International Conference on Basement Tectonics. Reidel, Netherlands (in press)
- Baker J, Bickle MJ, Buick IS, Holland TJB, Matthews A (1989) Isotopic and petrological evidence for the infiltration of water-rich fluids during the Miocene M2 metamorphism on Naxos, Greece. *Geochim Cosmochim Acta* 53:2037–2050
- Baumgartner LP, Ferry JM (1991) A model for coupled fluid-flow and mixed-volatile mineral reactions with applications to regional metamorphism. *Contrib Mineral Petrol* 106:273–285
- Baumgartner LP, Rumble D III (1988) Transport of stable isotopes: I: Development of a kinetic continuum theory for stable isotope transport. *Contrib Mineral Petrol* 98:417–430
- Berman RG (1988) Internally-consistent thermodynamic data for minerals in the system Na<sub>2</sub>O–K<sub>2</sub>O–CaO–MgO–FeO–Fe<sub>2</sub>O<sub>3</sub>–Al<sub>2</sub>O<sub>3</sub>–SiO<sub>2</sub>–TiO<sub>2</sub>–H<sub>2</sub>O–CO<sub>2</sub>. *J Petrol* 29:445–522
- Bickle M, Baker J (1990) Migration of reaction and isotopic fronts in infiltration zones: assessments of fluid flux in metamorphic terrains. *Earth Planet Sci Lett* 98:1–13
- Bickle MJ, McKenzie D (1987) The transport of heat and matter by fluids during metamorphism. *Contrib Mineral Petrol* 95:384–392
- Birch F (1966) Compressibility; elastic constants. In: Clark SP Jr (ed) Handbook of physical constants. *Mem Geol Soc Am* 97:97
- Blattner P, Lassey KR (1990) Transport of stable isotopes, kinetics, dispersive advection, and the 'isotopic fronts' of Baumgartner and Rumble (1988). *Contrib Mineral Petrol* 105:486–490
- Bottinga Y (1969) Calculated fractionation factors for carbon and hydrogen isotope exchange in the system calcite–CO<sub>2</sub>–graphite–methane–hydrogen and water vapour. *Geochim Cosmochim Acta* 33:49–64
- Bottinga Y (1968) Calculation of fractionation factors for carbon and oxygen exchange in the system calcite–carbon dioxide–water. *J Phys Chemistry* 72:800–808
- Brenan JM (1991) Development and maintenance of metamorphic permeability: implications for fluid transport. In: Kerrick DM (ed) Contact metamorphism. *Mineral Soc Reviews in Mineralogy* 26:291–320
- Bryndzia LT, Scott SD (1984) Experimentally determined activity model,  $\Delta H_f^0$ ,  $S_f^0$ , and  $\Delta G_f^0$  of iron chlorite [Fe<sub>5</sub>Al<sub>2</sub>Si<sub>3</sub>O<sub>10</sub>(OH)<sub>8</sub>]. *Abs Geol Soc Am* 16:458
- Chamberlain CP, Ferry JM, Rumble D III (1990) The effect of net-transfer reactions on the isotopic composition of minerals. *Contrib Mineral Petrol* 105:322–336
- Chacko T, Mayeda TK, Clayton RN, Goldsmith JR (1989) An experimental determination of <sup>18</sup>O/<sup>16</sup>O and <sup>13</sup>C/<sup>12</sup>C fractionations between CO<sub>2</sub> and calcite at 10 kbar. *Abs Geol Soc Am* 21:A11
- Chiba H, Chacko T, Clayton RN, Goldsmith JR (1989) Oxygen isotope fractionations involving diopside, forsterite, magnetite, and calcite: application to geothermometry. *Geochim Cosmochim Acta* 53:2985–2995
- Clayton RN, Mayeda TK (1963) The use of bromine pentafluoride in the extraction of oxygen from oxides and silicates for isotope analysis. *Geochim Cosmochim Acta* 27:43–52
- Clayton RN, O'Neil JR, Mayeda TK (1972) Oxygen isotope exchange between quartz and water. *J Geophys Res* 77:3057–3067
- Duffy CJ, Greenwood HJ (1979) Phase equilibria in the system MgO–MgF<sub>2</sub>–SiO<sub>2</sub>–H<sub>2</sub>O. *Am Mineral* 64:1156–1174
- Ferry JM (1991) Dehydration and decarbonation reactions as a record of fluid infiltration. In: Kerrick DM (ed) Contact metamorphism. *Mineral Soc Reviews in Mineralogy* 26:351–394
- Ferry JM (1983) On the control of temperature, fluid composition, and reaction progress during metamorphism. *Am J Sci* 283-A:201–232
- Fox LK, Miller DM (1990) Jurassic granitoids and related rocks of the southern Bristol Mountains, southern Providence Mountains, and Colton Hills, Mojave Desert, California. In: Anderson JL (ed) The nature and origin of cordilleran magmatism. *Mem Geol Soc Am* 174:111–132
- Gordon TM, Greenwood HJ (1970) The reaction: dolomite + quartz + water = talc + calcite + carbon dioxide. *Am J Sci* 268:225–242
- Guggenheim EA (1967) Thermodynamics: an advanced treatment for chemists and physicists. North-Holland Phys Pub, Amsterdam
- Hall DL, Cohen LH, Schiffman P (1988) Hydrothermal alteration associated with the Iron Hat iron skarn deposit, eastern Mojave Desert, San Bernardino County, California. *Econ Geol* 83:568–587
- Hickman SH, Evans B (1987) Influence of geometry upon crack healing rate in calcite. *Phys Chem Minerals* 15:91–102
- Holloway JR (1987) Igneous fluids. In: Carmichael ISE, Eugster HP (eds) Thermodynamic modeling of geological materials: minerals, fluids and melts. *Mineral Soc Reviews in Mineralogy* 17:211–233
- Holness MB, Graham CM (1991) Equilibrium dihedral angles in the system H<sub>2</sub>O–CO<sub>2</sub>–NaCl–calcite, and implications for fluid flow during metamorphism. *Contrib Mineral Petrol* 108:368–383
- Jacobs GK, Kerrick DM (1981) Methane: an equation of state with application to the ternary system H<sub>2</sub>O–CO<sub>2</sub>–CH<sub>4</sub>. *Geochim Cosmochim Acta* 45:607–614
- Kerrick DM, Jacobs GK (1981) A modified Redlich-Kwong equation for H<sub>2</sub>O, CO<sub>2</sub>, and H<sub>2</sub>O–CO<sub>2</sub> mixtures at elevated pressures and temperatures. *Am J Sci* 281:735–767
- Kerrick DM, Lasage AC, Raeburn SP (1991) Kinetics of heterogeneous reactions. In: Kerrick DM (ed) Contact metamorphism. *Mineral Soc Reviews in Mineralogy* 26:583–672
- Labotka TC (1991) Chemical and physical properties of fluids. In: Kerrick DM (ed) Contact metamorphism. *Mineral Soc Reviews in Mineralogy* 26:43–104
- Lamb WM, Valley JW (1985) C–O–H fluid calculations and granulite genesis. In: Tobi AC, Touret JLR (eds) The deep proterozoic crust of the North Atlantic Provinces. Reidel, Dordrecht, pp 119–131
- Matsuhisa Y, Goldsmith JR, Clayton RN (1979) Oxygen isotope fractionation in the system quartz–albite–anorthite–water. *Geochim Cosmochim Acta* 43:1131–1140
- Matthey DP, Taylor WR, Green DH, Pillinger CT (1990) Carbon isotopic fractionation between CO<sub>2</sub> vapour, silicate and carbonate melts: an experimental study to 30 kbar. *Contrib Mineral Petrol* 104:492–505
- McCrea JM (1950) On the isotope chemistry of carbonates and a paleotemperature scale. *J Chem Phys* 18:849–857
- Nabelek PI (1987) General equations for modeling fluid/rock interaction using trace elements and isotopes. *Geochim Cosmochim Acta* 51:1765–1769
- Naumov GB, Ryzhenko N, Khodakovskiy IL (1971) Handbook of thermodynamic data. In: Barnes I, Speltz V (eds) US Geol Survey Report WRD-74-001 (Russian translation), pp 1–328

- Ohmoto H (1972) Systematics of sulfur and carbon isotopes in hydrothermal ore deposits. *Econ Geol* 67:551–578
- Ohmoto H (1986) Stable isotope geochemistry of ore deposits. In: Valley JW, Taylor HP Jr, O'Neil JR (eds) Stable isotopes in high temperature geological processes. *Mineral Soc Am Reviews in Mineralogy* 16:491–559
- Ohmoto H, Kerrick D (1977) Devolatilization equilibria in graphitic systems. *Am J Sci* 277:1013–1044
- O'Neil JR, Clayton RN, Mayeda TK (1969) Oxygen isotope fractionation in divalent metal carbonates. *J Chem Physics* 51:5547–5558
- Pineau F, Javoy M (1983) Carbon isotopes and concentrations in mid-oceanic ridge basalts. *Earth Planet Sci Lett* 62:239–257
- Ribbe PH (1982) The humite series and Mn-analogs. In: Ribbe (ed) Orthosilicates. *Mineral Soc Reviews in Mineralogy* 5:231–274
- Rice JM (1980) Phase equilibria involving humite minerals in impure dolomitic limestones. *Contrib Mineral Petrol* 71:219–235
- Robei RA, Hemingway BS, Fisher JR (1979) Thermochemical properties of minerals and related substances at 298.15 K and 1 b ( $10^5$  Pa) pressure and at higher temperatures. *Bull US Geol Survey* 1452:1–456
- Rumble D III (1982) Stable isotope fractionation during metamorphic devolatilization reactions. In: Ferry JM (ed) Characterization of metamorphism through mineral equilibria. *Mineral Soc Reviews in Mineralogy* 10:327–352
- Sheppard SMF, Schwarcz HP (1970) Fractionation of carbon and oxygen isotopes and magnesium between metamorphic calcite and dolomite. *Contrib Mineral Petrol* 26:161–198
- Shettel DL Jr (1978) Experimental determination of oxygen isotopic fractionation between  $H_2O$  and hydrous silicate melts. PhD dissertation, Pennsylvania State University
- Skinner BJ (1966) Thermal expansion. In: Clark SP Jr (ed) *Handbook of physical constants*. *Mem Geol Soc Am* 97:78
- Skippen GB (1974) An experimental model for low pressure metamorphism of siliceous dolomitic marble. *Am J Sci* 274:487–509
- Stull DR, Prophet H (1971) JANAF thermochemical tables. NBS Nat Stand Ref Data Ser 37:1–1141
- Taylor BE (1986) Magmatic volatiles: isotopic variation in C, H, and S. In: Valley JW, Taylor HP Jr, O'Neil JR (eds) Stable isotopes in high temperature geological processes. *Mineral Soc Am Reviews in Mineralogy* 16:186–226
- Thompson JB Jr, Laird J, Thompson AB (1982) Reactions in amphibolite, greenschist and blueschist. *J Petrol* 23:1–27
- Valley JW, Peterson EU, Essene EJ, Bowman JR (1982) Fluorophlogopite and fluortremolite in Adirondack marbles and calculated C–O–H–F fluid compositions. *Am Mineral* 67:545–557
- Wachter EA, Hayes JM (1985) Exchange of oxygen isotopes in carbon dioxide-phosphoric acid systems. *Chem Geol* 52:356–374
- Watson EB, Brenan JM, Baker DR (1990) Distribution of fluids in the continental mantle. In: Menzies MA (ed) *Continental mantle*. Clarendon Press Oxford, pp 111–125
- Winter GA, Essene EJ, Peacor DR (1983) Mn-humites from Bald Knob, North Carolina: mineralogy and phase equilibria. *Am Mineral* 68:951–959
- Young ED (1990) Geothermobarometric and geochemical studies of two crystalline terrains of the eastern Mojave Desert, USA. PhD dissertation, University of Southern California, Los Angeles
- Young ED, Wooden JL, Shieh Y-N, Farber D (1992) Geochemical evolution of Jurassic diorites from the Bristol Lake region, California, USA and the role of assimilation. *Contrib Mineral Petrol* (in press)
- Young ED, Wooden JL (1988) Mid-crustal emplacement of Mesozoic granitoids, eastern Mojave Desert: evidence from crystallization barometry. *Abs Geol Soc Am* 20:139

Editorial responsibility: J. Ferry